

# Quantum Zeno Monte Carlo for observable measurement

Mancheon Han<sup>1</sup>, Hyowon Park<sup>2,3\*</sup>, Sangkook Choi<sup>1\*</sup>

<sup>1</sup>Department of Computational Sciences, Korea Institute For Advanced Study (KIAS), 85 Hoegiro Dongdaemun-gu, Seoul, 02455, Republic of Korea.

<sup>2</sup>Materials Science Division, Argonne National Laboratory, Argonne, IL, 60439, USA.

<sup>3</sup>Department of Physics, University of Illinois at Chicago, Chicago, IL, 60607, USA.

\*Corresponding author(s). E-mail(s): [hyowon@uic.edu](mailto:hyowon@uic.edu);  
[sangkookchoi@kias.re.kr](mailto:sangkookchoi@kias.re.kr);

Contributing authors: [mchan@kias.re.kr](mailto:mchan@kias.re.kr);

## Abstract

The advent of logical quantum processors marks the beginning of the early stages of error-corrected quantum computation. As a bridge between the noisy intermediate scale quantum (NISQ) era and the fault-tolerant quantum computing (FTQC) era, these devices and their successors have the potential to revolutionize the solution of classically challenging problems. An important application of quantum computers is to calculate observables of quantum systems. This problem is crucial for solving quantum many-body and optimization problems. However, due to limited error correction capabilities, this new era are still susceptible to noise, thereby necessitating new quantum algorithms with polynomial complexity as well as noise-resilience. This paper proposes a new noise-resilient and ansatz-free algorithm, called Quantum Zeno Monte Carlo. It utilizes the quantum Zeno effect and Monte Carlo integration for multi-step adiabatic transitions to the target eigenstates. It can efficiently find static as well as dynamic physical properties such as ground state energy, excited state energies, and Green's function without the use of variational parameters. This algorithm offers a polynomial computational cost and quantum circuit depth that is significantly lower than the quantum phase estimation.

**Keywords:** Quantum algorithm, quantum Zeno effect, Monte Carlo, Energy eigenvalues, Green's function

## 1 The onset of the error-corrected quantum computing era

The quantum computer [1–3] utilizes quantum algorithms to tackle computationally challenging problems, offering potential solutions to classically hard problems. A significant challenge lies in finding Hamiltonian eigenstates and their physical properties [4], crucial for material design and quantum machine learning implementation. By providing an initial state sufficiently close to the target eigenstate, this problem can be solved within polynomial quantum time [5, 6] with a fully fault-tolerant quantum computer (FTQC) [7, 8]. However, the preceding decades have been marked by the noisy intermediate-scale quantum (NISQ) era [9] rather than the FTQC era. Due to substantial device noise, quantum algorithms for NISQ systems prioritize noise resilience, leading to the dominance of ansatz-based algorithms [10, 11] without provable polynomial complexity.

The emergence of quantum devices with 48 logical qubits [12] marks the start of error-corrected quantum computing. These devices, along with their future advancements, have the potential to showcase quantum advantage, bridging the gap between NISQ and FTQC eras. Early error-corrected quantum computers are expected to handle longer quantum circuits than NISQ devices and execute quantum algorithms with polynomial complexity. However, algorithms designed for the FTQC era may not be suitable for early error-corrected quantum computers, as they still face device noise due to limited error corrections. As a result, developing new quantum algorithms that exhibit polynomial complexity and are resilient to noise shows promise for achieving quantum advantage in early error-corrected quantum computers.

We introduce the quantum Zeno Monte Carlo (QZMC) algorithm. This algorithm is robust against device noise as well as trotter error. Furthermore, this algorithm enables the computation of static as well as dynamic physical properties for quantum systems within polynomial quantum time. We validate its noise resilience by implementing it on IBM's NISQ devices for small systems. We also demonstrate its polynomial complexity using analytical approach and numerical demonstration on a noiseless quantum computer simulator. Interestingly, the maximum quantum circuit depth required is notably shorter than that of the quantum phase estimation algorithm [13, 14]. (See Supplementary Information for comparison with other methods [15–17].)

## 2 Quantum Zeno methods

The Quantum Zeno Monte Carlo algorithm draws inspiration from the quantum Zeno effect [18]. This is the phenomenon that repeated measurements slow down state transitions. We briefly outline this effect: A system varying with a continuous variable  $\lambda$  is

represented by the state  $|\psi_\lambda\rangle$ . Increasing  $\lambda$  to  $\lambda + \Delta\lambda$  yields the state  $|\psi_{\lambda+\Delta\lambda}\rangle$ , which remains  $|\psi_\lambda\rangle$  with a probability of  $|\langle\psi_\lambda|\psi_{\lambda+\Delta\lambda}\rangle|^2$ . Because its maximum is at  $\Delta\lambda = 0$ , this probability becomes  $1 - \mathcal{O}((\Delta\lambda)^2)$  for sufficiently small  $\Delta\lambda$ . By dividing  $\Delta\lambda$  into  $N$  slices and measuring at each interval of  $\Delta\lambda/N$ , the probability of measuring  $|\psi_\lambda\rangle$  at every step is  $1 - \mathcal{O}((\Delta\lambda)^2/N)$ . Increasing the measurement frequency  $N$  ensures the system remains in its initial state  $|\psi_\lambda\rangle$ .

While the original article [18] focused on state freezing through continuous measurements, the principle can also be applied to obtain an energy eigenstate by varying the Hamiltonian for each measurement [19–22]. Let's denote our target Hamiltonian as  $H$ , with its eigenstate as  $|\Phi\rangle$ . Suppose we have an easily preparable eigenstate  $|\Phi_0\rangle$  of  $H_0$  and the state is adiabatically connected to  $|\Phi\rangle$ . Due to the Van Vleck catastrophe [23, 24],  $|\Phi_0\rangle$  has very small overlap with  $|\Phi\rangle$  in general, potentially requiring a large number of measurements to obtain  $|\Phi\rangle$  directly from  $|\Phi_0\rangle$ . Instead, we consider measuring  $H_\alpha = (1 - \alpha/N_\alpha)H_0 + (\alpha/N_\alpha)H$  consecutively for  $\alpha = 1, \dots, N_\alpha$ . Utilizing the quantum Zeno principle, we can obtain  $|\Phi\rangle$  with very high probability as we increase the number of consecutive measurements  $N_\alpha$ .

### 3 Quantum Zeno Monte Carlo

The quantum Zeno principle can be implemented using projections, which is equivalent to measurements. Let's consider  $H_\alpha = (1 - \alpha/N_\alpha)H_0 + (\alpha/N_\alpha)H$ , where  $\alpha = 1, \dots, N_\alpha$ , and  $|\Phi_0\rangle$  is the eigenstate of  $H_0$  that can be readily prepared. For the eigenstate  $|\Phi_\alpha\rangle$  of  $H_\alpha$ , the operator that projects onto  $|\Phi_\alpha\rangle$  is represented as  $|\Phi_\alpha\rangle\langle\Phi_\alpha|$ . Then, the consecutive projections  $\mathcal{P}_\alpha$  applied to  $|\Phi_0\rangle$  is

$$|\Psi_\alpha\rangle = \mathcal{P}_\alpha |\Phi_0\rangle, \quad \mathcal{P}_\alpha = |\Phi_\alpha\rangle\langle\Phi_\alpha| \dots |\Phi_1\rangle\langle\Phi_1|, \quad (1)$$

which is equal to  $|\Phi_\alpha\rangle$  apart from the normalization. The quantum Zeno principle ensures that  $\langle\Psi_\alpha|\Psi_\alpha\rangle = \langle\Phi_0|\mathcal{P}_\alpha^\dagger\mathcal{P}_\alpha|\Phi_0\rangle$  approaches 1 as  $N_\alpha \rightarrow \infty$ . For the implementation of  $\mathcal{P}_\alpha$ , we use the approximate projection operator defined as

$$P_H^\beta(E) = \sum_j |j\rangle\langle j| e^{-\beta^2(\mathcal{E}_j - E)^2/2} = e^{-\beta^2(H - E)^2/2}, \quad (2)$$

while  $\mathcal{E}_j$  and  $|j\rangle$  are energy eigenvalues and eigenstates for a Hamiltonian  $H$ . As  $\beta$  increases, Eq. (2) becomes the projection onto the subspace with the energy  $E$ . Its implementation on the quantum computer can be achieved by using the Fourier expansion [25–28]

$$P_H^\beta(E) = \frac{1}{\sqrt{2\pi\beta^2}} \int_{-\infty}^{\infty} e^{-\frac{t^2}{2\beta^2}} e^{-i(H - E)t} dt. \quad (3)$$

The integrand in Eq. (3) represents the time evolution which can be implemented within a polynomial quantum time [29, 30]. Then, the consecutive projection  $\mathcal{P}_\alpha$  can

be approximated by

$$\mathcal{P}_\alpha^\beta = P_{H_\alpha}^\beta(E_\alpha) \dots P_{H_1}^\beta(E_1), \quad (4)$$

while  $E_\alpha$  is the energy eigenvalue of  $H_\alpha$  corresponds to  $|\Phi_\alpha\rangle$ . By substituting  $\mathcal{P}_\alpha$  by  $\mathcal{P}_\alpha^\beta$ , consecutive projection transforms into a multidimensional integral of consecutive time evolution, which can be computed using the Monte Carlo method [31]. Like recently proposed algorithms [25, 26], our objective is to compute the expectation values  $\langle O \rangle$  of observables rather than the state itself. By using  $|\Psi_\alpha\rangle$ ,  $\langle O \rangle_\alpha = \langle \Phi_\alpha | O | \Phi_\alpha \rangle$  can be determined as

$$\langle O \rangle_\alpha = \frac{\langle \Psi_\alpha | O | \Psi_\alpha \rangle}{\langle \Psi_\alpha | \Psi_\alpha \rangle}, \quad (5)$$

where  $\langle \Psi_\alpha | A | \Psi_\alpha \rangle$  for an arbitrary operator  $A$  is computed by the summation of consecutive time evolutions,

$$\frac{1}{N_\nu} \sum_\nu \langle \Phi_0 | e^{-iK_1 t_{\nu,2\alpha}} \dots e^{-iK_\alpha t_{\nu,\alpha+1}} A e^{-iK_\alpha t_{\nu,\alpha}} \dots e^{-iK_1 t_{\nu,1}} | \Phi_0 \rangle. \quad (6)$$

Here,  $K_{\alpha'} = H_{\alpha'} - E_{\alpha'}$  for  $\alpha' = 1, \dots, \alpha$  and we use  $N_\nu$  samples of  $\mathbf{t}_\nu = [t_{\nu,1} \ t_{\nu,2} \ \dots \ t_{\nu,2\alpha}]^T$ , where each  $t_{\nu,k}$  is drawn from the gaussian distribution with a standard deviation of  $\beta$ . Consequently, various static and dynamic properties of Hamiltonian eigenstates can be computed using the aforementioned quantum Zeno Monte Carlo (QZMC) method. Figure 1 provides a summary of QZMC. Our approach leverages the concept of the quantum Zeno effect, enabling the construction of unnormalized eigenstate  $|\Psi_\alpha\rangle$  of  $H$  from easily preparable  $|\Phi_0\rangle$ , as illustrated in Fig. 1a. Then, we compute the observable  $\langle \Phi_\alpha | O | \Phi_\alpha \rangle$  by expanding  $\langle \Psi_\alpha | O | \Psi_\alpha \rangle$  and  $\langle \Psi_\alpha | \Psi_\alpha \rangle$  as a summation of the consecutive time evolutions (Fig. 1b).

The QZMC computation relies on prior knowledge of energy eigenvalues  $E_\alpha$ . Therefore, a practical method for their computation is necessary. Here, we propose the predictor-corrector QZMC method for determining energy eigenvalues. Suppose we know  $E_0, E_1, \dots, E_{\alpha-1}$  and aim to compute  $E_\alpha$ . Similar to the predictor-corrector method used in solving differential equations [32], we begin with a rough estimate of  $E_\alpha$ , termed the predictor. Our predictor for  $E_\alpha$  is the first-order perturbation approximation [33], given by  $E_\alpha = E_{\alpha-1} + \langle \Phi_{\alpha-1} | h_{\alpha-1} | \Phi_{\alpha-1} \rangle$ , where  $h_{\alpha-1} = H_\alpha - H_{\alpha-1}$ . Subsequently, using the predictor  $E_\alpha$ , we compute a more accurate estimate of  $E_\alpha$ , termed the corrector. We determine the corrector based on the properties of the consecutive projection,

$$E_\alpha = E_{\alpha-1} + \frac{\langle \Psi_\alpha | \Phi_\alpha \rangle \langle \Phi_\alpha | h_{\alpha-1} | \Psi_{\alpha-1} \rangle}{\|\Psi_\alpha\|^2} \quad (\text{Corrector}). \quad (7)$$

This equation directly computes the energy difference  $E_\alpha - E_{\alpha-1}$  using QZMC. Compared to estimating the entire energy, this approach enhances robustness against

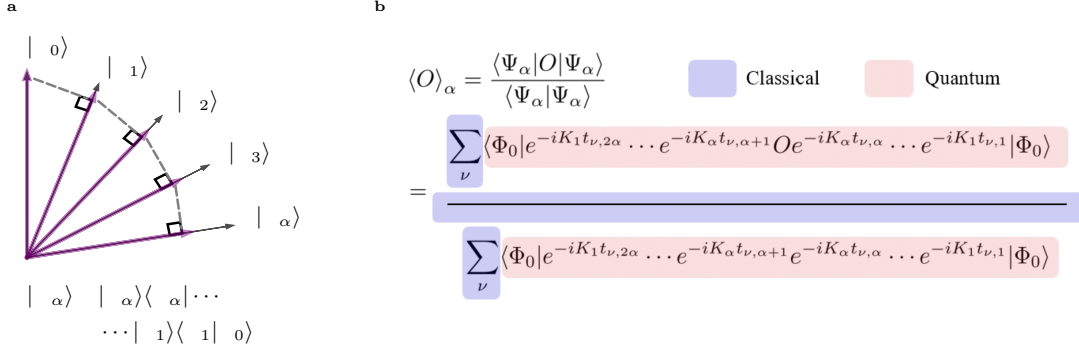


**Fig. 1 | Overview of the Quantum Zeno Monte Carlo.** **a** depicts the construction of the unnormalized eigenstate  $|\Psi_\alpha\rangle$  of  $H_\alpha$  from the eigenstate  $|\Phi_0\rangle$  of  $H_0$ . Each  $|\Phi_k\rangle$  represents the normalized eigenstate of  $H_k$ . In **b**, we present a summary of our Quantum Zeno Monte Carlo for computing the expectation value of an observable ( $O$ ). First, classical computer generates a time vector  $\mathbf{t}_\nu = [t_{\nu,1} \ t_{\nu,2} \ \dots \ t_{\nu,2\alpha}]^T$ , where  $t_{\nu,k}$  follows Gaussian distribution. Next, quantum computer measure the expectation value with the given time vector. Finally, the sum over  $N_\nu$  Monte Carlo sampling as well as the division is conducted by using classical computer. Here,  $K_{\alpha'}$  represents  $H_{\alpha'} - E_{\alpha'}$ .

noise by confining noise influences to the energy difference ( $E_\alpha - E_{\alpha-1}$ ) alone. Based on this insight, we employed Eq. (7), which can be computed as in Eq. (6) by substituting  $|\Phi_\alpha\rangle\langle\Phi_\alpha|$  by  $P_H^\beta(E_\alpha)$ . More details of QZMC as well as its extension to compute Green's function are described in the Supplementary Information.

## 4 QZMC on NISQ devices

Here, we demonstrate the noise resilience of our algorithm by simulating several systems on NISQ devices. We begin with eigenstates of  $H_0 = H(\lambda = 0)$ . Then, we create a discrete path from  $\lambda = 0$  to  $\lambda = 1$  with  $\lambda_\alpha = \alpha/N_\alpha$ , where  $N_\alpha = 10$ , and apply the predictor-corrector QZMC for  $H_\alpha = H(\lambda_\alpha)$ . The first system we consider (Figure 2) is the two-level system with the Hamiltonian,  $H(\lambda) = X/2 + (2\lambda - 1)Z$ . Next, we simulate the  $H_2$  molecule (Figure 3a) in the STO-3G basis [34], a typical testbed for quantum algorithms [35, 36]. By constraining the electron number to be 2 and the total spin to be 0 [37, 38], the system can be represented by a 2-qubit Hamiltonian. We calculate the energy spectrum of  $H_2$  as a function of interatomic distance ( $R$ ). Lastly, we consider the 2-site Hubbard model [39]. The Hubbard dimer (Figure 3b-f) at its half filling and singlet spin configuration can be mapped to a two-qubit Hamiltonian. Energy eigenvalues of the Hubbard dimer are computed by increasing onsite Coulomb interaction( $U$ ).

The two-level system results are displayed in Fig.2. Ground state energy as well as its expectation value of  $X$ ,  $Y$  and  $Z$  operators are displayed in Fig.2 a and b. Despite device noises in *ibmq\_lima*, measured observables match well with exact values (dashed lines). As shown in Fig.2c, computed ground state fidelity,

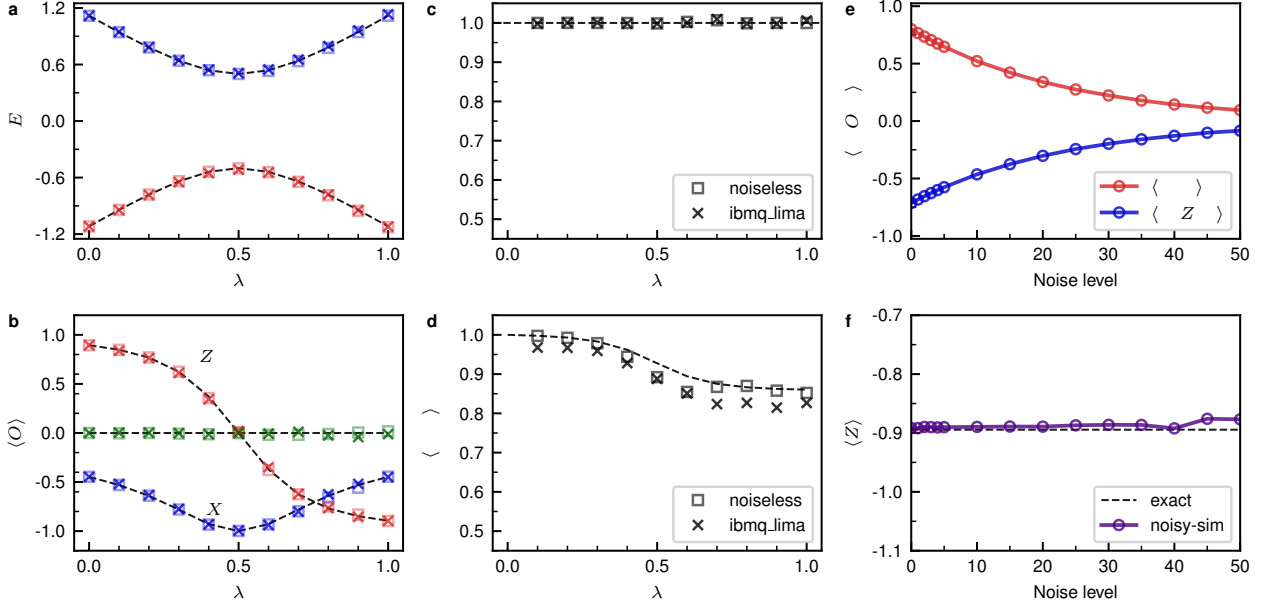


**Fig. 2 | A two level system.** The energy eigenvalues of the ground (red) and the excited state (blue) are plotted in **a**. In **b**, we plotted  $\langle X \rangle$  (blue),  $\langle Y \rangle$  (green), and  $\langle Z \rangle$  (red) calculated for the ground states. **c** and **d** display the fidelity  $\mathcal{F}$  and  $\langle \Psi | \Psi \rangle$  for the ground state. In **a-d**, dotted lines represent the exact result, boxes represent QZMC results with a noiseless simulator, and crosses represent results with *ibmq\_lima*. We plotted  $\langle \Psi | \Psi \rangle$ ,  $\langle \Psi | Z | \Psi \rangle$ , and  $\langle Z \rangle$  as a function of the noise level in **e** and **f**. The calculations for **e-f** are conducted with the qiskit noisy simulator using the noise model of *ibmq\_lima*. In this figure, we used  $\beta = 5$  and  $N_\nu = 400$ .

$\mathcal{F}_\alpha = |\langle \Phi_\alpha | \Psi_\alpha \rangle|^2 / \langle \Psi_\alpha | \Psi_\alpha \rangle$ , demonstrates accurate projection to the desired state by QZMC.

Interestingly,  $\langle \Psi | \Psi \rangle$  from the NISQ device, deviates largely from its exact value as well as the one from noiseless simulator, as shown in Fig.2d. This is in a sharp contrast to the agreement in the observables. To understand this discrepancy, we tested the dependence of the measured observables on the device noise magnitude using the qiskit [40] aer simulator. As shown in Figure.2e-f, as the noise level increases,  $\langle \Psi | \Psi \rangle$  decreases. Simultaneously, the absolute value of  $\langle \Psi | Z | \Psi \rangle$  (Fig.2e) also decreases. Surprisingly, these noise-induced errors cancel each other through the ratio of  $\langle \Psi | \Psi \rangle$  and  $\langle \Psi | Z | \Psi \rangle$ , so that  $\langle Z \rangle = \langle \Psi | Z | \Psi \rangle / \langle \Psi | \Psi \rangle$  (Fig.2f) remains robust against noise. Since quantum circuits for computing the numerator and denominator are nearly identical, division cancels out common noise effects, making the expectation value resilient to noise (See Supplementary Information for quantum circuits [41–43]).

Figure 3 presents computational results for two-qubit systems:  $H_2$  and the Hubbard dimer. We determined the energy eigenvalues of  $H_2$  within an error of 0.02 Ha using *ibmq\_lagos*. Energy eigenvalues for the Hubbard dimer are calculated within an error of  $0.06 t$  on *ibmq\_perth*, where  $t$  is electron hopping between two hubbard atoms. The

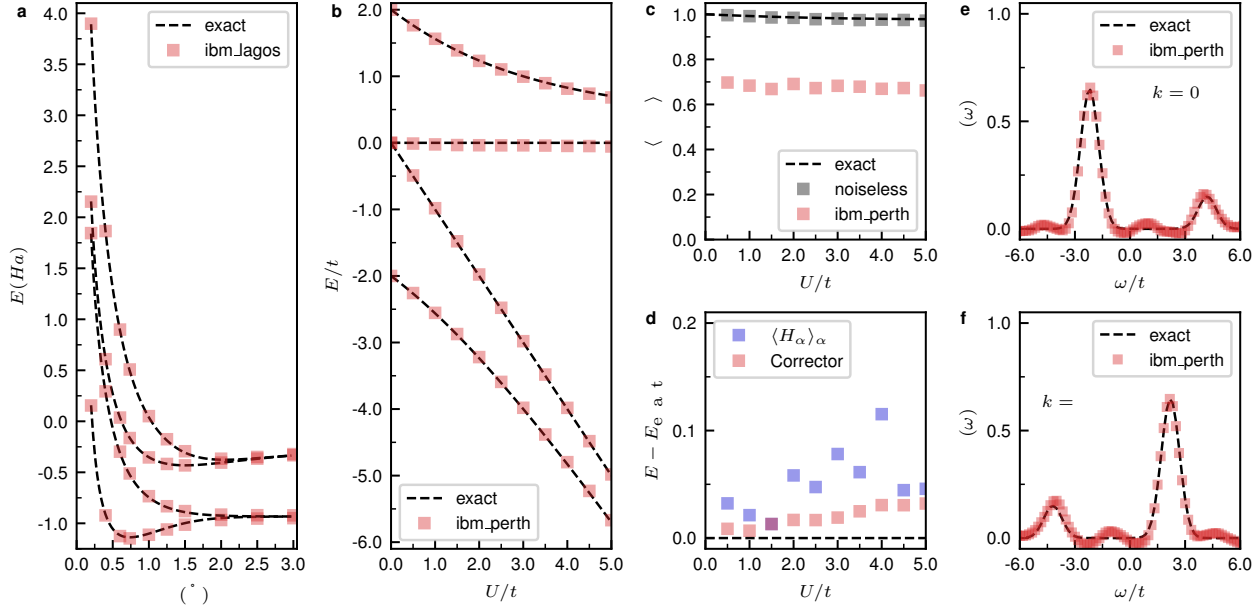


**Fig. 3** |  $\text{H}_2$  and the Hubbard dimer. **a** plots energy eigenvalues of  $\text{H}_2$  in a STO-3G basis as a function of the bond length. Here, we used  $\beta = 5$  and NISQ device calculation is conducted with *ibm\_lagos*. In **b-f**, we considered the Hubbard dimer. **b** shows energy eigenvalues as a function of the Coulomb interaction  $U$ . In **c**, we compared  $\langle \Psi | \Psi \rangle$  of the ground state calculated with the NISQ device with exact values and noiseless QZMC results. **d** compares two energy estimator  $\langle H_\alpha \rangle_\alpha$  and Eq. (7). The spectral functions for two different crystal momentum  $k = 0$  (**e**) and  $k = \pi$  (**f**) are plotted. For the Hubbard dimer, we used  $\beta = 0.5$  and *ibm\_perth* is used. In this figure, we used  $N_\nu = 100$  Monte Carlo samples for each  $\alpha$  and the spectral function is calculated with 300 Monte Carlo samples.

influences of device noise are much larger for two-qubit systems compared to one-qubit systems, leading to significant deviations in  $\langle \Psi | \Psi \rangle$  from exact values, as shown in Figure 3c.

However, as depicted in Figures 3a-b, eigenenergies are accurately reproduced despite large errors in  $\langle \Psi | \Psi \rangle$ . This is partly due to the noise cancellation through division. In addition to the noise cancellation effect demonstrated in Fig. 2 e-f, this noise resilience also rooted in the energy difference estimator Eq. (7). Fig. 3d shows that the formula in Eq. (7) for the estimator results in a smoother line compared to the formula for  $\langle H_\alpha \rangle_\alpha$ . Lastly, we compute the electronic spectral function  $A(\omega)$  [44] of the Hubbard dimer with the NISQ device. Figures 3e-f displays  $A(\omega)$  at  $k = 0$  and  $k = \pi$ , showing good agreements between exact values and measured values.

## 5 QZMC on large systems

We demonstrate polynomial complexity of our method by applying QZMC to large system with noiseless qsim-cirq [45] quantum computer simulator. We considered the

Hubbard model at the half-filling in various sizes. As  $H_0$ , we choose dimer array, featuring easily implementable non-degenerate ground state. We gradually increased the inter-dimer hopping  $t_{\text{inter}}$  from 0 to the desired value  $t$  as  $\alpha$  increased. We explored two geometries, chains and ladders, with periodic boundary conditions, as illustrated in Figure 4a. For each geometry, we computed systems with 6, 8, and 10 sites when  $U/t = 5$ . For QZMC, we used  $\beta = 3$ , with  $N_\alpha$  equal to the number of sites and  $N_\nu$  increases as  $h_\alpha$  increases. For the time evolution, we used the first order Trotterization [29, 46, 47], adjusting the Trotter steps as system changes. (See Supplementary information for the details on the choice of  $N_\nu$  and the number of Trotter steps).

Figure 4b illustrates the computed  $\langle \Psi | \Psi \rangle$  for the  $2 \times 5$  Hubbard model. Due to errors in the Trotter time evolution, the calculated  $\langle \Psi | \Psi \rangle$  significantly deviates from exact values. However, the ground state energy remains robust against Trotter errors due to the error cancellation through division, again. This robustness is comparable to its resilience against device noises, as demonstrated in Figure 4c. The figure shows that QZMC accurately reproduces the exact ground state energy across various configurations, from 6 to 10 sites, in both chain and ladder arrangements. Finally, we computed the local spectral function for Hubbard models and they are shown in Fig. 4d-g. Our results matches exact ones, accurately reproducing the positions and widths of every peak in the spectral functions.

## 6 Computational complexity

We analyzed the theoretical computational complexity of our method. To facilitate analysis, we adopt a uniform discretization approach, represented by  $H_\alpha = H_0 + (\alpha/N_\alpha)H'$  and focus solely on energy estimation complexity. The complexity of other observable measurement can be derived similarly (See Supplementary Information). Let's first examine the computational complexity of  $N_\nu$ . Our energy difference estimation in Eq. (7) involves a Monte Carlo summation of  $\langle \Phi_0 | U_1 H' U_2 | \Phi_0 \rangle$ , where  $U_1$  and  $U_2$  denote consecutive time evolutions. Since time evolution is unitary, each term in the summation is bounded by  $\|H'\|$ , resulting in a Monte Carlo error  $\epsilon$  bounded by  $\|H'\|/\sqrt{N_\nu}$ . Hence, the appropriate number of Monte Carlo samples  $N_\nu$  is proportional to  $\|H'\|^2/\epsilon^2$ . In most cases,  $H'$  can be represented as the sum of a polynomial number of Pauli strings [48], which gives  $\mathcal{O}(\text{poly}(n))$  upperbound of  $\|H'\|$ . Here  $n$  is the number of qubits. Therefore, we can state that  $N_\nu$  is  $\mathcal{O}(\text{poly}(n))/\epsilon^2$ . Next, let's consider  $N_\alpha$  which determines the total number of consecutive time evolutions. According to perturbation theory [33], each projection degrades the norm by about  $(\Delta\lambda)^2 \|H'\|^2/\Delta_g^2$ . Therefore, for a finite norm, we must have  $N_\alpha \propto \|H'\|^2/\Delta_g^2$ . Lastly, let's determine  $\beta$ , the width of each projection. For each projection, perturbative analysis shows that a projection error is proportional to  $\exp(-\beta^2 \Delta_g^2/2) \|H'\|/\Delta_g$ . To ensure this quantity is smaller than error  $\epsilon$ ,  $\beta$  must be proportional to  $\Delta_g^{-1} \sqrt{\log(\|H'\|/(\epsilon\Delta_g))}$ . Since the projection error is relative to the quantity of interest, the energy calculation by using Eq. (7) would have absolute error  $\epsilon$  if  $\beta$  is proportional to  $\Delta_g^{-1} \sqrt{\log(\|H'\|^2/(\epsilon\Delta_g))}$ . Because each of time evolution falls within the complexity class BQP (bounded-error

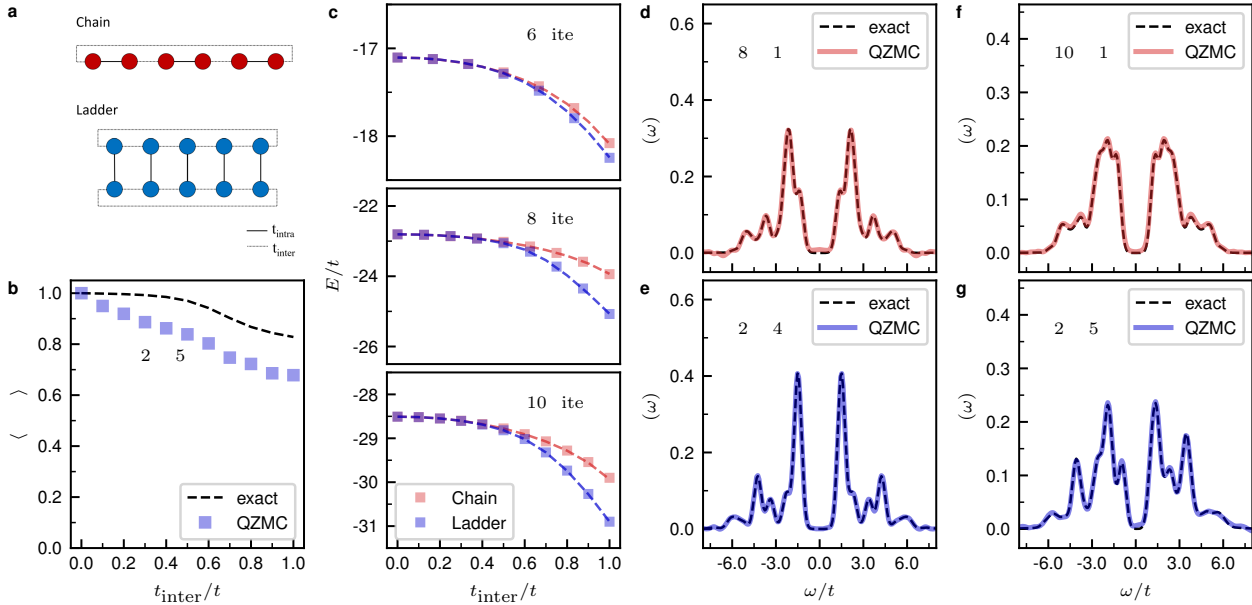


**Fig. 4 | The Hubbard model in various sizes.** **a** shows two geometries we considered, where colored circles denote sites, solid lines indicate intra-dimer hopping  $t_{\text{intra}}$ , and dotted lines represent inter-dimer hopping  $t_{\text{inter}}$ . **b** displays  $\langle \Psi | \Psi \rangle$  for the  $2 \times 5$  Hubbard model as a function of  $t_{\text{inter}}$ , while **c** presents ground state energy eigenvalues computed from QZMC. In each subplot of **c**, red squares denote energies for  $6 \times 1$ ,  $8 \times 1$ , and  $10 \times 1$  models with QZMC, with red dotted lines indicating corresponding exact values. Blue squares and lines represent the same values for  $2 \times 3$ ,  $2 \times 4$ , and  $2 \times 5$  cases. **d-g** depict the local spectral function for the Hubbard models.

quantum polynomial time) [49], we can conclude that QZMC provides energy eigenvalues and various physical properties within a polynomial quantum time, as long as the energy gap  $\Delta_g$  is finite.

## 7 Conclusion

In this work, we introduced the quantum Zeno Monte Carlo (QZMC) for the emerging stepping stone era of quantum computing [12]. This method computes static and dynamical observables of quantum systems within a polynomial quantum time. Leveraging the Quantum Zeno effect, we progressively approach the unknown eigenstate from the readily solvable Hamiltonian's eigenstate. This aspect distinguishes our method from other methods for phase estimations, which necessitate an initial state with significant overlap with the desired eigenstate [5, 6, 15, 17, 26, 27, 50]. Preparing a state with substantial overlap with an eigenstate of an easily solvable Hamiltonian is much simpler than preparing an initial state with non-trivial overlap with the unknown eigenstate, making our algorithm highly practical compared to other methods. Another characteristic of the algorithm is its computation of eigenstate properties

by dividing the properties of the unnormalized eigenstate by its norm squared (Eq. 5). We demonstrated that this approach effectively cancels out noise effects in both the denominator and the numerator, rendering the method resilient to device noise as well as Trotter error. This resilience arises from the similar noise levels experienced by both the denominator and the numerator of observable expectation value, leading us to conclude that our approach is well-suited for homogeneous parallel quantum computing.

## 8 Acknowledgment

We are grateful to Lin Lin for discussions with S.C. This research was supported by Quantum Simulator Development Project for Materials Innovation through the National Research Foundation of Korea (NRF) funded by the Korean government (Ministry of Science and ICT(MSIT))(No. NRF-2023M3K5A1094813). For one and two qubit simulations, we acknowledge the use of IBM Quantum services for this work and to advanced services provided by the IBM Quantum Researchers Program. The views expressed are those of the authors, and do not reflect the official policy or position of IBM or the IBM Quantum team. For larger system calculation, we used resources of the Center for Advanced Computation at Korea Institute for Advanced Study and the National Energy Research Scientific Computing Center (NERSC), a U.S. Department of Energy Office of Science User Facility operated under Contract No. DE-AC02-05CH11231. SC was supported by a KIAS Individual Grant (CG090601) at Korea Institute for Advanced Study. M.H. is supported by a KIAS Individual Grant (No. CG091301) at Korea Institute for Advanced Study.

## 9 Author contributions

M.H. conceived the original idea. M.H. and S.C. developed the idea into algorithms. M.H implemented and performed classical as well as quantum computer calculation. M.H. established the analytical proof of the computational complexity. All authors contributed to the writing of the manuscript.

## 10 Competing interests

The authors declare no competing interests.

## References

- [1] Benioff, P. The computer as a physical system: A microscopic quantum mechanical hamiltonian model of computers as represented by turing machines. *J. Stat. Phys.* **22**, 563–591 (1980).
- [2] Feynman, R. P. Simulating physics with computers. *Int. J. Theor. Phys.* **21** (1982).

- [3] Nielsen, M. A. & Chuang, I. L. *Quantum computation and quantum information* (Cambridge university press, 2010).
- [4] Shen, Y. *et al.* Estimating eigenenergies from quantum dynamics: A unified noise-resilient measurement-driven approach. Preprint at <https://arxiv.org/abs/2306.01858> (2023).
- [5] Kitaev, A. Y. Quantum measurements and the abelian stabilizer problem. Preprint at <https://arxiv.org/abs/quant-ph/9511026> (1995).
- [6] Abrams, D. S. & Lloyd, S. Quantum algorithm providing exponential speed increase for finding eigenvalues and eigenvectors. *Phys. Rev. Lett.* **83**, 5162 (1999).
- [7] Shor, P. W. Fault-tolerant quantum computation in Proc. 37th Conference on Foundations of Computer Science 56–65 (IEEE, 1996).
- [8] Gottesman, D. Theory of fault-tolerant quantum computation. *Phy. Rev. A* **57**, 127 (1998).
- [9] Preskill, J. Quantum Computing in the NISQ era and beyond. *Quantum* **2**, 79 (2018).
- [10] Peruzzo, A. *et al.* A variational eigenvalue solver on a photonic quantum processor. *Nat. Commun* **5**, 4213 (2014).
- [11] McClean, J. R., Romero, J., Babbush, R. & Aspuru-Guzik, A. The theory of variational hybrid quantum-classical algorithms. *New J. Phys.* **18**, 023023 (2016).
- [12] Bluvstein, D. *et al.* Logical quantum processor based on reconfigurable atom arrays. *Nature* **626**, 58–65 (2024).
- [13] Berry, D. W. *et al.* How to perform the most accurate possible phase measurements. *Phys. Rev. A* **80**, 052114 (2009).
- [14] Higgins, B. L., Berry, D. W., Bartlett, S. D., Wiseman, H. M. & Pryde, G. J. Entanglement-free heisenberg-limited phase estimation. *Nature* **450**, 393–396 (2007).
- [15] Lin, L. & Tong, Y. Heisenberg-limited ground-state energy estimation for early fault-tolerant quantum computers. *PRX Quantum* **3**, 010318 (2022).
- [16] Somma, R. D. Quantum eigenvalue estimation via time series analysis. *New J. Phys.* **21**, 123025 (2019).
- [17] Ding, Z. & Lin, L. Even shorter quantum circuit for phase estimation on early fault-tolerant quantum computers with applications to ground-state energy estimation. *PRX Quantum* **4**, 020331 (2023).

- [18] Misra, B. & Sudarshan, E. G. The zeno’s paradox in quantum theory. *J. Math. Phys.* **18**, 756–763 (1977).
- [19] Somma, R. D., Boixo, S., Barnum, H. & Knill, E. Quantum simulations of classical annealing processes. *Phys. Rev. Lett.* **101**, 130504 (2008).
- [20] Poulin, D. & Wocjan, P. Preparing ground states of quantum many-body systems on a quantum computer. *Phys. Rev. Lett.* **102**, 130503 (2009).
- [21] Boixo, S., Knill, E., Somma, R. D. *et al.* Eigenpath traversal by phase randomization. *Quantum Inf. Comput.* **9**, 833–855 (2009).
- [22] Lin, L. & Tong, Y. Optimal polynomial based quantum eigenstate filtering with application to solving quantum linear systems. *Quantum* **4**, 361 (2020).
- [23] Van Vleck, J. H. Nonorthogonality and ferromagnetism. *Phys. Rev.* **49**, 232–240 (1936).
- [24] Kohn, W. Nobel lecture: Electronic structure of matter—wave functions and density functionals. *Rev. Mod. Phys.* **71**, 1253–1266 (1999).
- [25] Zeng, P., Sun, J. & Yuan, X. Universal quantum algorithmic cooling on a quantum computer. Preprint at <https://arxiv.org/abs/2109.15304> (2021).
- [26] Huo, M. & Li, Y. Error-resilient Monte Carlo quantum simulation of imaginary time. *Quantum* **7**, 916 (2023).
- [27] Wang, G., França, D. S., Zhang, R., Zhu, S. & Johnson, P. D. Quantum algorithm for ground state energy estimation using circuit depth with exponentially improved dependence on precision. *Quantum* **7**, 1167 (2023).
- [28] Sun, J., Vilchez-Estevez, L., Vedral, V., Boothroyd, A. T. & Kim, M. Probing spectral features of quantum many-body systems with quantum simulators. Preprint at <https://arxiv.org/abs/2305.07649> (2023).
- [29] Lloyd, S. Universal quantum simulators. *Science* **273**, 1073–1078 (1996).
- [30] Zalka, C. Simulating quantum systems on a quantum computer. *Proceedings of the Royal Society of London. Series A: Mathematical, Physical and Engineering Sciences* **454**, 313–322 (1998).
- [31] Kroese, D. P., Taimre, T. & Botev, Z. I. *Handbook of Monte Carlo Methods* (John Wiley & Sons, 2011).
- [32] Heath, M. T. *Scientific computing: an introductory survey, revised second edition* (SIAM, 2018).

- [33] Landau, L. D. & Lifshitz, E. M. *Quantum mechanics: non-relativistic theory* Vol. 3 (Elsevier, 2013).
- [34] Stewart, R. F. Small gaussian expansions of slater-type orbitals. *J. Chem. Phys.* **52**, 431–438 (1970).
- [35] O’Malley, P. J. J. *et al.* Scalable quantum simulation of molecular energies. *Phys. Rev. X* **6**, 031007 (2016).
- [36] Motta, M. *et al.* Determining eigenstates and thermal states on a quantum computer using quantum imaginary time evolution. *Nat. Phys.* **16**, 205–210 (2020).
- [37] Seeley, J. T., Richard, M. J. & Love, P. J. The bravyi-kitaev transformation for quantum computation of electronic structure. *J. Chem. Phys.* **137** (2012).
- [38] Steudtner, M. & Wehner, S. Fermion-to-qubit mappings with varying resource requirements for quantum simulation. *New J. Phys.* **20**, 063010 (2018).
- [39] Hubbard, J. & Flowers, B. H. Electron correlations in narrow energy bands. *Proc. R. Soc. London, Ser. A* **276**, 238–257 (1963).
- [40] <https://www.ibm.com/quantum/qiskit>.
- [41] Shende, V. V., Markov, I. L. & Bullock, S. S. Minimal universal two-qubit controlled-not-based circuits. *Phys. Rev. A* **69**, 062321 (2004).
- [42] Shende, V., Bullock, S. & Markov, I. Synthesis of quantum-logic circuits. *IEEE Transactions on Computer-Aided Design of Integrated Circuits and Systems* **25**, 1000–1010 (2006).
- [43] Cross, A. W., Bishop, L. S., Sheldon, S., Naton, P. D. & Gambetta, J. M. Validating quantum computers using randomized model circuits. *Phys. Rev. A* **100**, 032328 (2019).
- [44] Negele, J. W. & Orland, H. *Quantum many-particle systems* Advanced book classics (Westview, Boulder, CO, 1988).
- [45] <https://quantumai.google/qsim>.
- [46] Trotter, H. F. On the product of semi-groups of operators. *Proc. Am. Math. Soc.* **10**, 545–551 (1959).
- [47] Layden, D. First-order trotter error from a second-order perspective. *Phys. Rev. Lett.* **128**, 210501 (2022).
- [48] Tilly, J. *et al.* The variational quantum eigensolver: A review of methods and best practices. *Phys. Rep.* **986**, 1–128 (2022).

- [49] Watrous, J. Quantum computational complexity. Preprint at <https://arxiv.org/abs/0804.3401> (2008).
- [50] Ni, H., Li, H. & Ying, L. On low-depth algorithms for quantum phase estimation. *Quantum* **7**, 1165 (2023).

# Supplementary information for "Quantum Zeno Monte Carlo for observable measurement"

Mancheon Han<sup>1</sup>, Hyowon Park<sup>2,3\*</sup>, Sangkook Choi<sup>1\*</sup>

<sup>1\*</sup>Department of Computational Sciences, Korea Institute For Advanced Study (KIAS), 85 Hoegiro Dongdaemun-gu, Seoul, 02455, Republic of Korea.

<sup>2\*</sup>Materials Science Division, Argonne National Laboratory, Argonne, IL, 60439, USA.

<sup>3\*</sup>Department of Physics, University of Illinois at Chicago, Chicago, IL, 60607, USA.

\*Corresponding author(s). E-mail(s): [hyowon@uic.edu](mailto:hyowon@uic.edu);  
[sangkookchoi@kias.re.kr](mailto:sangkookchoi@kias.re.kr);  
 Contributing authors: [mchan@kias.re.kr](mailto:mchan@kias.re.kr);

In this supplementary information, we discuss details of the methods and calculations in the main text. Then, we discuss the initial state preparation for the QZMC and compare our approach with others.

## 1 Quantum Zeno Monte Carlo

This section discuss details of the quantum Zeno Monte Carlo.

### 1.1 Static observables

First, we show the derivation of Eq. (6). By substituting  $\mathcal{P}_\alpha$  by  $\mathcal{P}_\alpha^\beta$ ,  $\langle \Psi_\alpha | A | \Psi_\alpha \rangle = \langle \Phi_0 | \mathcal{P}_\alpha^\dagger A \mathcal{P}_\alpha | \Phi_0 \rangle$  becomes

$$\langle \Psi_\alpha | A | \Psi_\alpha \rangle = \frac{1}{(2\pi\beta^2)^\alpha} \int_{-\infty}^{\infty} \dots \int_{-\infty}^{\infty} e^{-\sum_{a=1}^{2\alpha} \frac{t_a^2}{2\beta^2} + i\phi_\alpha(\mathbf{t})} z_\alpha(A, \mathbf{t}) dt_1 \dots dt_{2\alpha},$$

$$z_\alpha(A, \mathbf{t}) = \langle \Phi_0 | e^{-iH_1 t_{2\alpha}} \dots e^{-iH_\alpha t_{\alpha+1}} A e^{-iH_\alpha t_\alpha} \dots e^{-iH_1 t_1} | \Phi_0 \rangle,$$

$$\phi_\alpha(\mathbf{t}) = \sum_{\alpha'=1}^{\alpha} E_{\alpha'}(t_{\alpha'} + t_{2\alpha+1-\alpha'}). \quad (\text{S.1})$$

This multi-dimensional integration can be efficiently calculated by using the Monte Carlo method [31] with  $\{t_a \sim \mathcal{N}(0, \beta)\}$ . This yields Eq. (6). The measurement of  $z_\alpha(O, \mathbf{t})$  is achieved through the Pauli string [48] expansion of operator  $O$ . Similarly,  $\langle \Psi_\alpha | \Psi_\alpha \rangle = \langle \Psi_\alpha | \mathbb{I} | \Psi_\alpha \rangle$  becomes

$$\langle \Psi_\alpha | \Psi_\alpha \rangle = \frac{1}{(2\pi\beta^2)^\alpha} \int_{-\infty}^{\infty} \dots \int_{-\infty}^{\infty} e^{-\sum_{a=1}^{2\alpha} \frac{t_a^2}{2\beta^2} + i\phi_\alpha(\mathbf{t})} z_\alpha(\mathbb{I}, \mathbf{t}) dt_1 \dots dt_{2\alpha}. \quad (\text{S.2})$$

So it is computed as in Eq. (6). Then, the expectation value of the observable  $O$  is obtained by

$$\langle O \rangle_\alpha = \frac{\langle \Psi_\alpha | O | \Psi_\alpha \rangle}{\langle \Psi_\alpha | \Psi_\alpha \rangle}. \quad (\text{S.3})$$

## 1.2 Green's function

Next, we derive the Quantum Zeno Monte Carlo method for computing the electronic Green's function. The computation of other Green's function, such as the spin-spin correlation function, follows a similar approach. The retarded electronic Green's function is defined as  $G_{jk}^R(t) = -i\theta(t) \langle \Phi | \{c_j(t), c_k^\dagger(0)\} | \Phi \rangle$ , where  $\{, \}$  represents the anticommutator and  $c_j$  ( $c_j^\dagger$ ) is the annihilation (creation) operator for the  $j$ -th orbital. This Green's function is expressed compactly using the spectral function  $A_{jk}(\omega)$ ,

$$G_{jk}^R(\omega + i0^+) = \int_{-\infty}^{\infty} \frac{A_{jk}(\omega')}{\omega + i0^+ - \omega'} d\omega'. \quad (\text{S.4})$$

The spectral function  $A_{jk}(\omega)$  is expanded in [44]

$$\begin{aligned} A_{jk}(\omega) &= A_{jk,1}(\omega) + A_{jk,2}(\omega), \\ A_{jk,1}(\omega) &= \sum_m \langle \Phi | c_j | m \rangle \langle m | c_k^\dagger | \Phi \rangle \delta(\mathcal{E}_m - \mathcal{E}_\Phi - \omega), \\ A_{jk,2}(\omega) &= \sum_m \langle \Phi | c_k^\dagger | m \rangle \langle m | c_j | \Phi \rangle \delta(\mathcal{E}_m - \mathcal{E}_\Phi + \omega). \end{aligned} \quad (\text{S.5})$$

While  $|m\rangle$  and  $\mathcal{E}_m$  are the energy eigenstate and corresponding energy eigenvalue. We focus on computing  $A_{jk,1}(\omega)$ , as  $A_{jk,2}(\omega)$  can be computed similarly. The dirac delta function  $\delta(x)$  is approximated using the gaussian function  $1/\sqrt{2\pi\sigma^2} e^{-x^2/2\sigma^2}$ . So, with the gaussian broadening,  $A_{jk,1}(\omega)$  is computed as

$$A_{jk,1}(\omega) = \frac{1}{\sqrt{2\pi\sigma^2}} \sum_m \langle \Phi | c_j | m \rangle \langle m | c_k^\dagger | \Phi \rangle e^{-(\mathcal{E}_m - \mathcal{E}_\Phi - \omega)^2/2\sigma^2}$$

$$= \frac{1}{\sqrt{2\pi\sigma^2}} \langle \Phi | c_j e^{-(H - \mathcal{E}_\Phi - \omega)^2 / 2\sigma^2} c_k^\dagger | \Phi \rangle. \quad (\text{S.6})$$

For QZMC, we consider the Green's function at  $\alpha$ . Then, like Eq. (S.3), we can represent  $A_{jk,1}(\omega)$  as

$$A_{jk,1}(\omega) = \frac{1}{\sqrt{2\pi\sigma^2}} \frac{\tilde{A}_{jk,1}(\omega)}{\langle \Psi_\alpha | \Psi_\alpha \rangle}, \quad \tilde{A}_{jk,1}(\omega) = \langle \Psi_\alpha | c_j e^{-(H_\alpha - E_\alpha - \omega)^2 / 2\sigma^2} c_k^\dagger | \Psi_\alpha \rangle. \quad (\text{S.7})$$

By fourier expansion of  $e^{-(H_\alpha - E_\alpha - \omega)^2}$ , we can compute  $\tilde{A}_{jk,1}$  like Eq. (6),

$$\tilde{A}_{jk,1}(\omega) = \frac{1}{N_\nu} \sum_\nu g_\alpha(c_j, c_k^\dagger, \mathbf{t}_\nu) e^{i\phi_\alpha(\mathbf{t}_\nu, \omega)}, \quad (\text{S.8})$$

while  $g_\alpha(O_1, O_2, \mathbf{t}) = \langle \Phi_0 | e^{-iH_1 t_{2\alpha+1}} \dots e^{-iH_\alpha t_{\alpha+2}} O_1 e^{-iH_\alpha t_{\alpha+1}} O_2 e^{-iH_\alpha t_\alpha} \dots e^{-iH_1 t_1} | \Phi_0 \rangle$  and  $\phi_\alpha(\mathbf{t}, \omega) = \sum_{\alpha'=1}^\alpha E_{\alpha'}(t_{\alpha'} + t_{2\alpha+2-\alpha'}) + (E_\alpha + \omega)t_{\alpha+1}$ . Here,  $t_{\nu, \alpha+1} \sim \mathcal{N}(0, 1/\sigma)$  and  $t_{\nu, l} \sim \mathcal{N}(0, \beta)$  for all  $l \neq \alpha+1$ . Since  $g_\alpha(O_1, O_2, \mathbf{t})$  is not dependent on  $\omega$ , we can compute  $A_{jk}(\omega)$  for any  $\omega$  by storing  $g_\alpha(c_j, c_k^\dagger, \mathbf{t}_\nu)$ .

### 1.3 Corrector for the energy difference

The energy difference formula, Eq. (7), can be derived as follows.

$$\begin{aligned} E_\alpha &= \frac{\langle \Phi_0 | \mathcal{P}_\alpha^\dagger H_\alpha \mathcal{P}_\alpha | \Phi_0 \rangle}{\langle \Phi_0 | \mathcal{P}_\alpha^\dagger \mathcal{P}_\alpha | \Phi_0 \rangle} \\ &= \frac{\langle \Phi_0 | \mathcal{P}_\alpha^\dagger | \Phi_\alpha \rangle \langle \Phi_\alpha | H_\alpha \mathcal{P}_{\alpha-1} | \Phi_0 \rangle}{\langle \Phi_0 | \mathcal{P}_\alpha^\dagger \mathcal{P}_\alpha | \Phi_0 \rangle} \\ &= \frac{\langle \Phi_0 | \mathcal{P}_\alpha^\dagger | \Phi_\alpha \rangle \langle \Phi_\alpha | (H_{\alpha-1} + h_{\alpha-1}) \mathcal{P}_{\alpha-1} | \Phi_0 \rangle}{\langle \Phi_0 | \mathcal{P}_\alpha^\dagger \mathcal{P}_\alpha | \Phi_0 \rangle} \\ &= E_{\alpha-1} + \frac{\langle \Psi_\alpha | \Phi_\alpha \rangle \langle \Phi_\alpha | h_{\alpha-1} | \Psi_{\alpha-1} \rangle}{\langle \Psi_\alpha | \Psi_\alpha \rangle}. \end{aligned} \quad (\text{S.9})$$

By following same steps as obtaining Eq. (6), we obtain the Monte Carlo formula of the numerator,

$$\begin{aligned} \langle \Psi_\alpha | \Phi_\alpha \rangle \langle \Phi_\alpha | h_{\alpha-1} | \Psi_{\alpha-1} \rangle &= \frac{1}{N_\nu} \sum_\nu \hat{z}_\alpha(h_{\alpha-1}, \mathbf{t}_\nu) e^{i\phi_\alpha(\mathbf{t}_\nu)} \\ \hat{z}_\alpha(O, \mathbf{t}) &= \langle \Phi_0 | e^{-iH_1 t_{2\alpha}} \dots e^{-iH_\alpha t_{\alpha+1}} e^{-iH_\alpha t_\alpha} O \dots e^{-iH_1 t_1} | \Phi_0 \rangle, \end{aligned} \quad (\text{S.10})$$

while  $\phi_\alpha(\mathbf{t}) = \sum_{\alpha'=1}^\alpha E_{\alpha'}(t_{\alpha'} + t_{2\alpha+1-\alpha'})$ .

### 1.4 Computational complexity of QZMC

This section provides details on the complexity analysis of our method, which is briefly outline in the main text. We consider the hamiltonian  $H(\lambda) = H_0 + \lambda H'$ . And we begin

with  $|\Phi_0\rangle$ , an eigenstate of the  $H_0 = H(\lambda = 0)$  with eigenvalue  $E_0$ . For simplicity, we assume that  $|\Phi(\lambda)\rangle$ , adiabatically connected to  $|\Phi_0\rangle$ , is non-degenerate and has an eigenvalue  $E(\lambda)$  satisfying  $|E(\lambda) - \mathcal{E}_m| \geq \Delta_g$  for all eigenenergies of  $\mathcal{E}_m$  of  $H(\lambda)$  other than  $E(\lambda)$ . We then consider  $H_\alpha = H(\lambda_\alpha)$ ,  $\alpha = 1, \dots, N_\alpha$  with  $\lambda_\alpha = \alpha/N_\alpha$ , as in the main text. We denote  $E_\alpha = E(\lambda_\alpha)$ ,  $|\Phi_\alpha\rangle = |\Phi(\lambda_\alpha)\rangle$ .

#### 1.4.1 $N_\alpha$

First, we compute  $N_\alpha$  using exact projection. Utilizing perturbation theory [33], we have

$$\begin{aligned} \langle \Phi_\alpha | \Phi_{\alpha+1} \rangle &= \left( 1 - \frac{(\Delta\lambda)^2}{2} \sum_{m_\alpha \neq \Phi_\alpha} \frac{|\langle m_\alpha | H' | \Phi_\alpha \rangle|^2}{(E_\alpha - \mathcal{E}_{m,\alpha})^2} \right), \\ \langle m_\alpha | \Phi_{\alpha+1} \rangle &= \Delta\lambda \frac{\langle m_\alpha | H' | \Phi_\alpha \rangle}{E_\alpha - \mathcal{E}_{m,\alpha}} \text{ for } m_\alpha \neq \Phi_\alpha, \end{aligned} \quad (\text{S.11})$$

up to the leading order of  $\Delta\lambda = \lambda_{\alpha+1} - \lambda_\alpha$ . Here,  $|m_\alpha\rangle$  represent an eigenstate of  $H_\alpha$  with an eigenvalue of  $\mathcal{E}_{m,\alpha}$ . However,

$$\sum_{m_\alpha \neq \Phi_\alpha} \frac{|\langle m_\alpha | H' | \Phi_\alpha \rangle|^2}{(E_\alpha - \mathcal{E}_{m,\alpha})^2} \leq \sum_{m_\alpha \neq \Phi_\alpha} \frac{|\langle m_\alpha | H' | \Phi_\alpha \rangle|^2}{\Delta_g^2} \leq \frac{1}{\Delta_g^2} \|H'\|^2. \quad (\text{S.12})$$

Here, we employ the matrix norm induced by vector 2-norm [32],  $\|A\| = \sup_{\|x\|=1} \|Ax\|$ . Combining Eq. (S.11) and Eq. (S.12), we obtain

$$\langle \Psi_\alpha | \Psi_\alpha \rangle = |\langle \Phi_0 | \Phi_1 \rangle|^2 \dots |\langle \Phi_{\alpha-1} | \Phi_\alpha \rangle|^2 \geq 1 - \frac{\|H'\|^2}{\Delta_g^2} \frac{1}{N_\alpha}. \quad (\text{S.13})$$

Thus, we have  $\|\Psi_\alpha\|^2 \geq 1 - \eta_0$  for all  $\alpha$  by setting

$$N_\alpha \geq \frac{\|H'\|^2}{\Delta_g^2} \frac{1}{\eta_0}. \quad (\text{S.14})$$

#### 1.4.2 $\beta$

The impact of finite  $\beta$  on the projected state is described by

$$|\delta\Psi_\alpha^\beta\rangle = (\mathcal{P}_\alpha^\beta - \mathcal{P}_\alpha) |\Phi_0\rangle. \quad (\text{S.15})$$

Here, we show

$$\|\delta\Psi_\alpha^\beta\| \leq \frac{\alpha}{N_\alpha} e^{-\beta^2 \Delta_g^2 / 2} \frac{\|H'\|}{\Delta_g} \quad (\text{S.16})$$

inductively, where  $\|\delta\Psi_\alpha^\beta\|^2 = \langle \delta\Psi_\alpha^\beta | \delta\Psi_\alpha^\beta \rangle$ . First, we address the case of  $\alpha = 1$ . Employing the perturbation approach as in Eq.(S.11), we obtain

$$\begin{aligned}\|\delta\Psi_1^\beta\|^2 &= \langle \Phi_0 | (P_{H_1}^\beta(E_1) - |\Phi_1\rangle\langle\Phi_1|)^2 | \Phi_0 \rangle \\ &= (\Delta\lambda)^2 \sum_{m_1 \neq \Phi_1} e^{-\beta^2(\mathcal{E}_{m,1} - E_1)^2} \frac{|\langle \Phi_1 | H' | m_1 \rangle|^2}{(\mathcal{E}_{m,1} - E_1)^2} \\ &\leq (\Delta\lambda)^2 e^{-\beta^2\Delta_g^2} \frac{\|H'\|^2}{\Delta_g^2}\end{aligned}\quad (\text{S.17})$$

So,  $\|\delta\Psi_1^\beta\| \leq \frac{1}{N_\alpha} e^{-\beta^2\Delta_g^2/2} \frac{\|H'\|}{\Delta_g}$ . Suppose for  $\alpha$ ,  $\|\delta\Psi_\alpha^\beta\| \leq \frac{\alpha}{N_\alpha} e^{-\beta^2\Delta_g^2/2} \frac{\|H'\|}{\Delta_g}$ . Then,

$$|\delta\Psi_{\alpha+1}^\beta\rangle = (P_{\alpha+1}^\beta - |\Phi_{\alpha+1}\rangle\langle\Phi_{\alpha+1}|) |\Psi_\alpha\rangle + P_{\alpha+1}^\beta |\delta\Psi_\alpha^\beta\rangle. \quad (\text{S.18})$$

For simplicity, we expressed  $P_{\alpha+1}^\beta = P_{H_{\alpha+1}}^\beta(E_{\alpha+1})$ . Thus,

$$\begin{aligned}\|\delta\Psi_{\alpha+1}^\beta\|^2 &= \langle \Psi_\alpha | (P_{\alpha+1}^\beta - |\Phi_{\alpha+1}\rangle\langle\Phi_{\alpha+1}|)^2 | \Psi_\alpha \rangle \\ &\quad + \langle \Psi_\alpha | (P_{\alpha+1}^\beta - |\Phi_{\alpha+1}\rangle\langle\Phi_{\alpha+1}|) P_{\alpha+1}^\beta |\delta\Psi_\alpha^\beta\rangle \\ &\quad + \langle \delta\Psi_\alpha | P_{\alpha+1}^\beta (P_{\alpha+1}^\beta - |\Phi_{\alpha+1}\rangle\langle\Phi_{\alpha+1}|) | \Psi_\alpha \rangle + \langle \delta\Psi_\alpha | (P_{\alpha+1}^\beta)^2 | \delta\Psi_\alpha^\beta \rangle.\end{aligned}\quad (\text{S.19})$$

The first term is smaller than  $(\Delta\lambda)^2 e^{-\beta^2\Delta_g^2} \frac{\|H'\|^2}{\Delta_g^2}$  by following the same procedure as with Eq. (S.17). And the last term is smaller than  $\|\delta\Psi_\alpha^\beta\|^2 \leq \frac{\alpha^2}{N_\alpha^2} e^{-\beta^2\Delta_g^2} \frac{\|H'\|^2}{\Delta_g^2}$  since  $P_\alpha^\beta$  has eigenvalues smaller than 1. Consider the second term. Then,

$$\begin{aligned}&|\langle \Psi_\alpha | (P_{\alpha+1}^\beta - |\Phi_{\alpha+1}\rangle\langle\Phi_{\alpha+1}|) P_{\alpha+1}^\beta |\delta\Psi_\alpha^\beta\rangle| \\ &\leq \Delta\lambda \sum_{\substack{m_{\alpha+1} \\ \neq \Phi_{\alpha+1}}} \frac{|\langle \Phi_{\alpha+1} | H' | m_{\alpha+1} \rangle|}{|\mathcal{E}_{m,\alpha+1} - E_{\alpha+1}|} e^{-\beta^2(\mathcal{E}_{m,\alpha+1}^2 - E_{\alpha+1}^2)} | \langle m_{\alpha+1} | \delta\Psi_\alpha^\beta \rangle | \\ &\leq \Delta\lambda \frac{e^{-\beta^2\Delta_g^2}}{\Delta_g} \|H' | \Phi_{\alpha+1} \rangle\| \|\delta\Psi_\alpha^\beta\| \\ &\leq \Delta\lambda \frac{e^{-\beta^2\Delta_g^2}}{\Delta_g} \|H'\| \|\delta\Psi_\alpha^\beta\| \leq \Delta\lambda \frac{\alpha}{N_\alpha} e^{-\beta^2\Delta_g^2} \frac{\|H'\|^2}{\Delta_g^2}.\end{aligned}\quad (\text{S.20})$$

Similar argument provides the same bound for the third term. By using  $\Delta\alpha = 1/N_\alpha$ , we have

$$\|\delta\Psi_{\alpha+1}^\beta\|^2 \leq \frac{(\alpha+1)^2}{N_\alpha^2} e^{-\beta^2\Delta_g^2} \frac{\|H'\|^2}{\Delta_g^2}, \quad (\text{S.21})$$

which proves Eq. (S.16). So,  $|\langle \Psi_\alpha | \Psi_\alpha \rangle - \langle \Psi_\alpha^\beta | \Psi_\alpha^\beta \rangle|$  becomes smaller than  $\delta\eta$  by using

$$\beta \geq \frac{1}{\Delta_g} \sqrt{2 \log \left( \frac{\|H'\|}{\Delta_g} \frac{2}{\delta\eta} \right)}. \quad (\text{S.22})$$

If we are interested in the expectation value of the observable  $O$ ,  $\langle \Psi_\alpha^\beta | O | \Psi_\alpha^\beta \rangle$  has an error of

$$\delta \langle \Psi_\alpha^\beta | O | \Psi_\alpha^\beta \rangle = \langle \delta \Psi_\alpha^\beta | O | \Psi_\alpha \rangle + \langle \Psi_\alpha | O | \delta \Psi_\alpha^\beta \rangle + \langle \delta \Psi_\alpha^\beta | O | \delta \Psi_\alpha^\beta \rangle. \quad (\text{S.23})$$

which is smaller than

$$2 \|\delta \Psi_\alpha^\beta\| \|O\| + \|\delta \Psi_\alpha^\beta\|^2 \|O\|. \quad (\text{S.24})$$

By considering error up to the first order of  $\|\delta \Psi_\alpha^\beta\|$ , we have

$$\delta \langle \Psi_\alpha^\beta | O | \Psi_\alpha^\beta \rangle \leq 2 \|\delta \Psi_\alpha^\beta\| \|O\|. \quad (\text{S.25})$$

Then, the error of the expectation value  $\langle \Psi_\alpha^\beta | O | \Psi_\alpha^\beta \rangle / \langle \Psi_\alpha^\beta | \Psi_\alpha^\beta \rangle$  is estimated by

$$\begin{aligned} \delta \left( \frac{\langle \Psi_\alpha^\beta | O | \Psi_\alpha^\beta \rangle}{\langle \Psi_\alpha^\beta | \Psi_\alpha^\beta \rangle} \right) &= \frac{\delta \langle \Psi_\alpha^\beta | O | \Psi_\alpha^\beta \rangle}{\langle \Psi_\alpha | \Psi_\alpha \rangle} + \frac{\langle \Psi_\alpha | O | \Psi_\alpha \rangle}{\langle \Psi_\alpha | \Psi_\alpha \rangle^2} \delta \langle \Psi_\alpha^\beta | \Psi_\alpha^\beta \rangle \\ &\leq 4 \frac{\|\delta \Psi_\alpha^\beta\|}{\langle \Psi_\alpha | \Psi_\alpha \rangle} \|O\|, \end{aligned} \quad (\text{S.26})$$

because  $\langle \Psi_\alpha | O | \Psi_\alpha \rangle / \langle \Psi_\alpha | \Psi_\alpha \rangle \leq \|O\|$ . So, if  $\langle \Psi_\alpha | \Psi_\alpha \rangle \geq 1 - \eta$ ,  $\langle O \rangle$  can be estimated within an error of  $\epsilon$  by using

$$\beta \geq \frac{1}{\Delta_g} \sqrt{2 \log \left( \frac{\|H'\|}{\Delta_g} \frac{4 \|O\|}{1 - \eta} \frac{1}{\epsilon} \right)}. \quad (\text{S.27})$$

The energy estimator in Eq. (7) is a slightly different case since we are computing the energy difference at each  $\alpha$ . With finite  $\beta$ , the numerator in Eq. (7) have an error of

$$\langle \Psi_\alpha^\beta | P_{\alpha+1}^\beta P_{\alpha+1}^\beta (H_{\alpha+1} - H_\alpha - (E_{\alpha+1} - E_\alpha)) | \Psi_\alpha^\beta \rangle. \quad (\text{S.28})$$

Here, we considered error at  $\alpha+1$  in Eq. (7) instead of  $\alpha$  for the notational simplicity. Up to first order of  $\Delta\lambda$  and  $\|\delta \Psi_\alpha^\beta\|$ , above equation is equal to

$$\begin{aligned} &\langle \delta \Psi_\alpha^\beta | P_{\alpha+1}^\beta P_{\alpha+1}^\beta (H_{\alpha+1} - H_\alpha - (E_{\alpha+1} - E_\alpha)) | \Psi_\alpha \rangle \\ &+ \langle \Psi_\alpha | P_{\alpha+1}^\beta P_{\alpha+1}^\beta (H_{\alpha+1} - H_\alpha - (E_{\alpha+1} - E_\alpha)) | \delta \Psi_\alpha^\beta \rangle. \end{aligned} \quad (\text{S.29})$$

By using  $H_{\alpha+1} - H_\alpha = \Delta\lambda H'$  and  $E_{\alpha+1} - E_\alpha = \Delta\lambda E'_\alpha + \mathcal{O}(\Delta\lambda^2)$ , Eq. (S.29) is equal to

$$\Delta\lambda(\langle \delta\Psi_\alpha^\beta | P_{\alpha+1}^\beta P_{\alpha+1}^\beta (H' - E'_\alpha) | \Psi_\alpha \rangle + \langle \Psi_\alpha | P_{\alpha+1}^\beta P_{\alpha+1}^\beta (H' - E'_\alpha) | \delta\Psi_\alpha^\beta \rangle), \quad (\text{S.30})$$

which is smaller than

$$4\Delta\lambda \|\delta\Psi_\alpha^\beta\| \|H'\|, \quad (\text{S.31})$$

as  $E'_\alpha \leq \|H'\|$ . If  $\|\Psi_\alpha^\beta\|^2 \geq 1 - \eta$ , each energy difference estimator has the error no greater than

$$4\Delta\lambda \frac{\|\delta\Psi_\alpha^\beta\| \|H'\|}{1 - \eta} \leq 4 \frac{\alpha}{N_\alpha^2} e^{-\beta^2 \Delta_g^2 / 2} \frac{\|H'\|^2}{\Delta_g} \frac{1}{1 - \eta}. \quad (\text{S.32})$$

Thus, the energy estimation  $E_\alpha$  has the error bound of

$$2 \frac{\alpha(\alpha - 1)}{N_\alpha^2} e^{-\beta^2 \Delta_g^2 / 2} \frac{\|H'\|^2}{\Delta_g} \frac{1}{1 - \eta}, \quad (\text{S.33})$$

which increases as  $\alpha$  increase and is smaller than  $2e^{-\beta^2 \Delta_g^2 / 2} \frac{\|H'\|^2}{\Delta_g} \frac{1}{1 - \eta}$ . So, we can compute the energy within an error of  $\epsilon$  by using

$$\beta \geq \frac{1}{\Delta_g} \sqrt{2 \log \left( \frac{2\|H'\|^2}{\Delta_g} \frac{1}{1 - \eta} \frac{1}{\epsilon} \right)}. \quad (\text{S.34})$$

### 1.4.3 $N_\nu$

Consider a random variable  $\mathbf{t}$  with a continuous probability distribution  $g(\mathbf{t})$ . The expectation value of  $x(\mathbf{t})$  is given by

$$\mathbb{E}[x] = \int x(\mathbf{t})g(\mathbf{t})d\mathbf{t}. \quad (\text{S.35})$$

The variance of the  $x$  is calculated as

$$\text{Var}[x] = \mathbb{E}[x^2] - (\mathbb{E}[x])^2. \quad (\text{S.36})$$

If  $|x(\mathbf{t})| \leq L$  for all  $\mathbf{t}$ , we have  $\mathbb{E}[x^2] \leq L^2$ , which gives

$$\sigma_x^2 = \text{Var}[x] \leq L^2 - (\mathbb{E}[x])^2 \leq L^2. \quad (\text{S.37})$$

Consequently, if we generate  $N_\nu$  samples of  $\mathbf{t}$  and use the average of  $x(\mathbf{t})$  as our estimator  $\bar{x}$  of  $\mathbb{E}[x]$ , standard error  $\sigma_{\bar{x}}$  of  $\bar{x}$  is bounded by  $\frac{L}{\sqrt{N_\nu}}$  [31]. This discussion extends to for Eq. (6) with  $L = \|A\|$ . The observable expectation Eq. (5) can be seen as  $\bar{x}$  divided by  $\bar{y}$ , where  $|x(\mathbf{t})| \leq L$  and  $|y(\mathbf{t})| \leq 1$ . Then, by using the the delta

method [31] and independent sampling of  $\mathbf{t}$  for  $\bar{x}$  and  $\bar{y}$ , the variance  $\sigma_{\bar{x}/\bar{y}}^2$  of  $\bar{x}/\bar{y}$  is estimated as

$$\sigma_{\bar{x}/\bar{y}}^2 = \frac{1}{\bar{y}^2} \left( \sigma_{\bar{x}}^2 + \frac{\bar{x}^2}{\bar{y}^2} \sigma_{\bar{y}}^2 \right) \leq \frac{1}{\bar{y}^2} \left( \frac{L^2}{N_\nu} + \frac{\bar{x}^2}{\bar{y}^2} \frac{1}{N_\nu} \right) \leq \frac{L^2}{N_\nu \bar{y}^2} \left( 1 + \frac{1}{\bar{y}^2} \right). \quad (\text{S.38})$$

Therefore, the standard error  $\sigma_{\langle O \rangle_\alpha}$  of  $\langle O \rangle_\alpha$  becomes

$$\sigma_{\langle O \rangle_\alpha} \leq \frac{\|O\|}{\sqrt{N_\nu}} \frac{1}{\langle \Psi_\alpha^\beta | \Psi_\alpha^\beta \rangle} \sqrt{1 + \frac{1}{\langle \Psi_\alpha^\beta | \Psi_\alpha^\beta \rangle^2}}. \quad (\text{S.39})$$

Similarly, the energy difference calculated by Eq. (S.10) has a standard error of

$$\sigma_{E_\alpha - E_{\alpha-1}} \leq \Delta \lambda \frac{\|H'\|}{\sqrt{N_\nu}} \frac{1}{\langle \Psi_\alpha^\beta | \Psi_\alpha^\beta \rangle} \sqrt{1 + \frac{1}{\langle \Psi_\alpha^\beta | \Psi_\alpha^\beta \rangle^2}}. \quad (\text{S.40})$$

#### 1.4.4 The number of shots, $N_s$

In real quantum computers, the estimation of unitary expectation value involves with a finite number  $N_s$  of repetitions of the same circuits, commonly referred as shots. This introduces statistical errors with a standard deviation of  $1/\sqrt{N_s}$  to each measurement. Consequently, when measuring observable  $\langle O \rangle$  using the pauli string expansion, the finite number of shots modifies Eq. (S.39) to

$$\sigma_{\langle O \rangle_\alpha} \leq \frac{1}{\sqrt{N_\nu}} \left( \|O\| + \frac{\sqrt{\sum_\gamma o_\gamma^2}}{\sqrt{N_s}} \right) \frac{1}{\langle \Psi_\alpha^\beta | \Psi_\alpha^\beta \rangle} \sqrt{1 + \frac{1}{\langle \Psi_\alpha^\beta | \Psi_\alpha^\beta \rangle^2}}, \quad (\text{S.41})$$

where  $O = \sum_\gamma o_\gamma P_\gamma$  represents a pauli string expansion of  $O$ . Similarly, Eq. (S.40) transforms to

$$\sigma_{E_\alpha - E_{\alpha-1}} \leq \Delta \lambda \frac{1}{\sqrt{N_\nu}} \left( \|H'\| + \frac{\sqrt{\sum_\gamma w_\gamma^2}}{\sqrt{N_s}} \right) \frac{1}{\langle \Psi_\alpha^\beta | \Psi_\alpha^\beta \rangle} \sqrt{1 + \frac{1}{\langle \Psi_\alpha^\beta | \Psi_\alpha^\beta \rangle^2}}. \quad (\text{S.42})$$

Here,  $H' = \sum_\gamma w_\gamma P_\gamma$  stands as a pauli string expansion of  $H'$ .

#### 1.4.5 Complexity of the energy estimation

In this section, we explore the complexity of obtaining the energy eigenvalue with an additive error of  $\epsilon$  by determining suitable computational parameters  $N_\alpha$ ,  $\beta$ , and  $N_\nu$ . Similarly, complexities for observable calculations can be derived. The computational complexity of the quantum algorithm is mainly influenced by the circuit depth and the number of repetitions. To quantify the circuit depth, we examine the distribution of the consecutive time evolution length  $L_\nu = |t_{\nu,1}| + \dots + |t_{\nu,2N_\alpha}|$ . Since

each  $|t_{\nu,1}|, \dots, |t_{\nu,2N_\alpha}|$  follows a half-normal distribution with a mean of  $\beta\sqrt{2/\pi}$  and a standard deviation of  $\beta\sqrt{1-2/\pi}$ ,  $L_\nu$  has a mean  $2N_\alpha\beta\sqrt{2/\pi}$  and a standard deviation of  $\sqrt{2N_\alpha}\beta\sqrt{1-2/\pi}$ . As a measure of the maximum time evolution length, we employ  $C_{90}N_\alpha\beta$ , where the probability of  $L_\nu$  being smaller than  $C_{90}N_\alpha\beta$  is 90%.  $C_{90}$  is numerically determined by testing the cumulative distribution of  $L_\nu$ , and it monotonically decreases as  $N_\alpha$  increases. For  $N_\alpha = 1$ ,  $C_{90} = 2.7545$ , which reduces to 2.0978 at  $N_\alpha = 5$ , and eventually approaches  $2\sqrt{2/\pi}$  as  $N_\alpha \rightarrow \infty$ .

Then,  $\beta$  and  $N_\alpha$  determines the circuit depth. We find appropriate values for  $\beta$  and  $N_\alpha$  by ensuring that  $\langle \Psi_\alpha^\beta | \Psi_\alpha^\beta \rangle \geq 1 - \eta$ , where  $\eta = 0.5$ , in order to limit error amplification. To achieve this, we set  $\eta_0 = 0.4$  in Eq. (S.14) and  $\delta\eta$  in Eq. (S.22) to 0.1, resulting in  $\eta = \eta_0 + \delta\eta = 0.5$ . Considering an energy error of  $\epsilon$  in Eq. (S.34), this gives

$$N_\alpha\beta \geq 2.5 \frac{\|H'\|^2}{\Delta_g^3} \sqrt{2 \log \left( \max \left( \frac{4\|H'\|^2}{\Delta_g} \frac{1}{\epsilon}, \frac{20\|H'\|}{\Delta_g} \right) \right)}. \quad (\text{S.43})$$

So, in terms of  $n$ , the number of qubits, we have the maximum evolution time of

$$C_{90}N_\alpha\beta = \mathcal{O}(\Delta_g^{-3} \text{poly}(n)) \sqrt{\log(\mathcal{O}(\Delta_g^{-1}\epsilon^{-1} \text{poly}(n)))}. \quad (\text{S.44})$$

Next, we consider the number of repetitions. Given that we compute  $N_\nu$  circuits with  $N_s$  shots each, the total number of repetitions is  $N_\nu N_s$ . Utilizing Eq. (S.42) with  $\langle \Psi_\alpha^\beta | \Psi_\alpha^\beta \rangle \geq 1 - \eta = 0.5$ , we can compute Eq. (7) within an error of  $\epsilon$  with the Monte Carlo samples

$$N_\nu \geq \left( \|H'\| + \frac{\sqrt{\sum_\gamma w_\gamma^2}}{\sqrt{N_s}} \right)^2 \frac{20}{\epsilon^2} \quad (\text{S.45})$$

for each  $\alpha$ . By fixing  $N_s$ , we find  $N_\nu = \mathcal{O}(\epsilon^{-2} \text{poly}(n))$ , as  $\|H'\|^2$  and  $\sum_\gamma w_\gamma^2$  are  $\mathcal{O}(\text{poly}(n))$ . Consequently, the total number of repetitions required to obtain the energy eigenvalue within an error of  $\epsilon$  is

$$N_\nu N_s = \mathcal{O}(\epsilon^{-2} \text{poly}(n)). \quad (\text{S.46})$$

Table. 1 summarize and compare the computational complexity of our method with other methods.

## 1.5 The effect of the inaccurate energy eigenvalues

In practical calculations, we encounter a finite error  $\delta$  in energy estimation. The effect of this energy error is  $e^{-\beta^2\delta^2}$  for each projection. However, this effect cancels out for the calculation of the expectation values and the energy difference formula. Thus, one should only consider that

$$e^{-2N_\alpha\beta^2\delta^2} \quad (\text{S.47})$$

**Table 1** Computational complexity of QZMC and other quantum algorithms

	Maximum time evolution length	Repetitions
QZMC	$\mathcal{O}(\Delta_g^{-3} \text{poly}(n))\sqrt{\log(\mathcal{O}(\Delta_g^{-1}\epsilon^{-1} \text{poly}(n)))}$	$\mathcal{O}(\epsilon^{-2} \text{poly}(n))$
QPE [13, 14]	$\tilde{\mathcal{O}}(\epsilon^{-1} p_0^{-1})$	$\tilde{\mathcal{O}}(p_0^{-1} \text{polylog}(\epsilon^{-1}))$
QEEA [16]	$\tilde{\mathcal{O}}(\epsilon^{-1} \text{polylog}(p_0^{-1}))$	$\tilde{\mathcal{O}}(\epsilon^{-3} p_0^{-2})$
Ref. [15]	$\tilde{\mathcal{O}}(\epsilon^{-1} \text{polylog}(p_0^{-1}))$	$\tilde{\mathcal{O}}(p_0^{-2} \text{polylog}(\epsilon^{-1}))$
Ref. [27]	$\mathcal{O}(\Delta_g^{-1} \text{polylog}(\epsilon^{-1} p_0^{-1} \Delta_g))$	$\mathcal{O}(p_0^{-2} \epsilon^{-2} \Delta_g^2)$

This table summarize the complexity of QZMC to compute energy eigenvalues and compares it with several other quantum algorithms that computes energy eigenvalues within a single ancilla qubit. Complexity analysis of QPE and QEEA imported from Ref. [15]. Here,  $p_0$  the probability of getting exact eigenstate from the initial states,  $\epsilon$  is a desired precision in the energy, and  $n$  is the number of qubits. Optimized algorithms for highly overlapped initial states [17, 50] shows similar dependence with algorithm of Ref. [15], only constant factor is different.

is not too small to completely destroy  $\langle \Psi_\alpha^\beta | \Psi_\alpha^\beta \rangle$ . To ensure that this value is greater than  $1/2$ , we require  $\beta$  to satisfy

$$\beta \leq \frac{1}{\delta} \sqrt{\frac{\log 2}{2N_\alpha}}. \quad (\text{S.48})$$

## 1.6 Quantum Circuits for QZMC

We illustrate several quantum circuits utilized in the quantum Zeno Monte Carlo (QZMC) method. Figure S.1 depicts the QZMC circuits employing controlled time-evolution. If noise is too large so that the noise that **a-c** experience are significantly different to each other, we can use **d** for the calculation of  $\langle \Psi | \Psi \rangle$  instead of **a** to mitigate the influence of the noise. QZMC with the circuits shown in Fig. S.1 is general and applicable for any Hamiltonian. However, it may suffer from substantial device noise due to numerous controlled-time evolutions. To circumvent this, we can adopt the quantum circuits depicted in Figure S.2. This approach eliminates the need for controlled time-evolution when a common eigenstate  $|\Phi_{\text{ref}}\rangle$  exists for  $H_1, \dots, H_{N_\alpha}$ . While this appears to be a stringent restriction, many practical physical and chemical systems possess such a common eigenstate, such as the vacuum. For the Green's function calculation, we have to compute  $g_\alpha$  in Eq. (S.8). Through the pauli string decomposition, this translates into a weighted sum of  $\langle \Phi_0 | e^{-iH_1 t_{2\alpha+1}} \dots e^{-iH_\alpha t_{\alpha+2}} P_\gamma e^{-iH_\alpha t_{\alpha+1}} P_{\gamma'} e^{-iH_\alpha t_\alpha} \dots e^{-iH_1 t_1} | \Phi_0 \rangle$ . Therefore, the Green's function calculation can be executed using the quantum circuits depicted in Figure S.3.

## 2 Details of NISQ calculations

In this section, we describe details of NISQ simulations considered in the main text. Throughout the NISQ simulations, we used  $N_s = 4000$ .

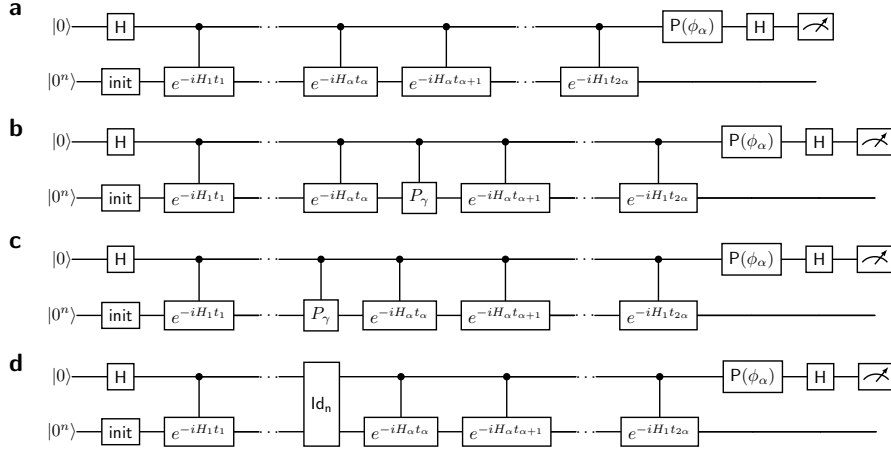


**Fig. S.1 | Quantum circuits for QZMC without a reference state.** **a** is the circuit for  $\langle \Psi | \Psi \rangle$ , **b** for  $\langle \Psi | O | \Psi \rangle$ , and **c** for  $\langle \Psi_\alpha | \Phi_\alpha \rangle \langle \Phi_\alpha | h_{\alpha-1} | \Psi_{\alpha-1} \rangle$ . The noise effect difference in  $\langle \Psi | \Psi \rangle$  and  $\langle \Psi_\alpha | \Phi_\alpha \rangle \langle \Phi_\alpha | h_{\alpha-1} | \Psi_{\alpha-1} \rangle$  can be reduced by using the circuit **d**, which contains noisy identity that mimics the noise effect of controlled- $P_\gamma$ , instead of **a**. The circuit **init** refers the circuit that transforms  $|0^n\rangle$  to  $|\Phi_0\rangle$ .

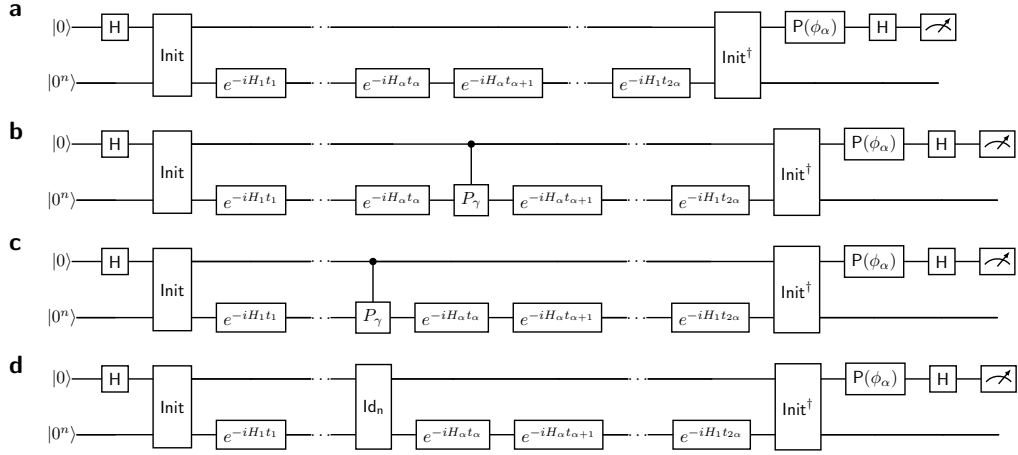


**Fig. S.2 | Quantum circuits for QZMC with a reference state.** **a** is the circuit for  $\langle \Psi | \Psi \rangle$ , **b** for  $\langle \Psi | O | \Psi \rangle$ , and **c** for  $\langle \Psi_\alpha | \Phi_\alpha \rangle \langle \Phi_\alpha | h_{\alpha-1} | \Psi_{\alpha-1} \rangle$ . **d** is the circuit for the  $\langle \Psi | \Psi \rangle$  that includes noisy identity  $\text{Id}_n$ , making noise effect on  $\langle \Psi | \Psi \rangle$  and  $\langle \Psi_\alpha | \Phi_\alpha \rangle \langle \Phi_\alpha | h_{\alpha-1} | \Psi_{\alpha-1} \rangle$  similar to each other. The circuit **init** transforms  $|0^n\rangle$  to a reference state  $|\Phi_{\text{ref}}\rangle$  if the control qubit is at  $|0\rangle$ , and  $|0^n\rangle$  to  $|\Phi_0\rangle$  if the control qubit is at  $|1\rangle$ .

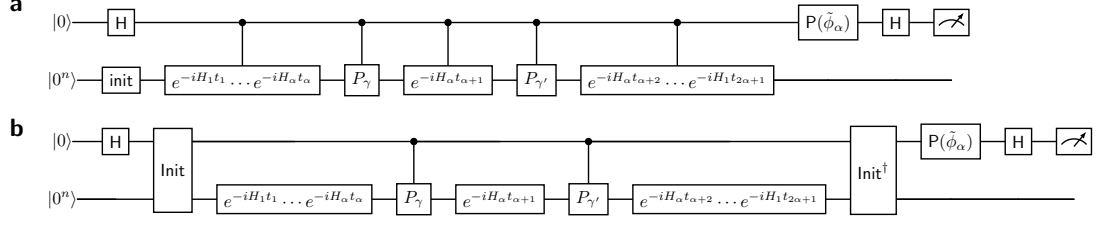


**Fig. S.3 | Quantum circuits for Green's function.** **a** is the circuit without a reference state, **b** is the circuit with a reference state.  $\tilde{\phi}_\alpha = \phi_\alpha$  for a real part,  $\tilde{\phi}_\alpha = \phi_\alpha - \pi/2$  for an imaginary part.

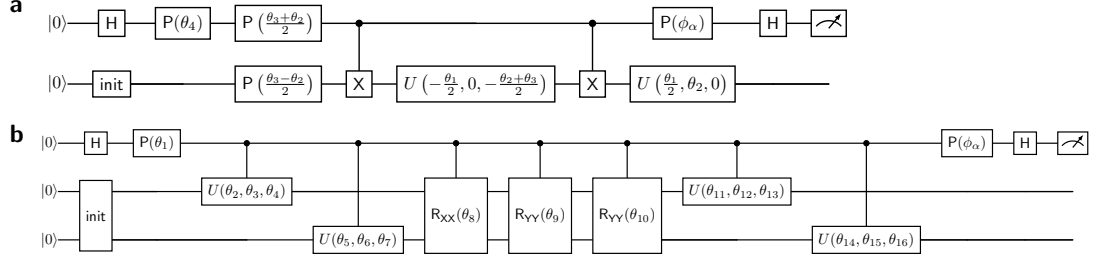


**Fig. S.4 | Quantum circuits for QZMC that uses 1 and 2 qubit circuit compression** **a** is the compressed circuit for 1-qubit systems, and **b** is the compressed circuit for 2-qubit systems.

## 2.1 Compressed quantum circuit

First, we present the compressed circuits for the 1 and 2 qubit systems, used for computations in Fig. 2-3. Because any 1 and 2 qubit unitary can be represented with a few operations [41], we can use compressed circuits Figure S.4 instead of Fig. S.1 or Fig. S.2 for those cases. For the 1-qubit system, parameters  $\theta$  for the unitary matrix  $U$  is found from [41]

$$U = e^{i\theta_4} \begin{bmatrix} \cos(\theta_1/2) & -\sin(\theta_1/2)e^{i\theta_3} \\ \sin(\theta_1/2)e^{i\theta_2} & \cos(\theta_1/2)e^{i(\theta_2+\theta_3)} \end{bmatrix}. \quad (\text{S.49})$$

For the 2-qubit system, we used the two-qubit Weyl decomposition [43] as implemented in the qiskit.

## 2.2 Two-level system

In the main text, we investigated the two level system described by the Hamiltonian  $H(\lambda) = X/2 + (2\lambda - 1)Z$ , traversing from  $\lambda = 0$  to  $\lambda = 1$  via a discrete path with  $\lambda_\alpha = \alpha/N_\alpha$ . Here, with noiseless simulator, we assess the parameter dependencies of QZMC by varying  $N_\alpha$  and  $\beta$ , and also evaluating the impact of finite trotterization steps. Figure S.5 illustrates these dependencies for  $\langle \Psi | \Psi \rangle$  and the ground state energy  $E$  of  $H(\lambda = 1)$ . **a** and **b** of Fig. S.5 demonstrate the  $\beta$  dependence. This reveals an increasing accuracy with  $\beta$  until  $\beta = 10$ . Large error for  $\beta > 10$  can be understood

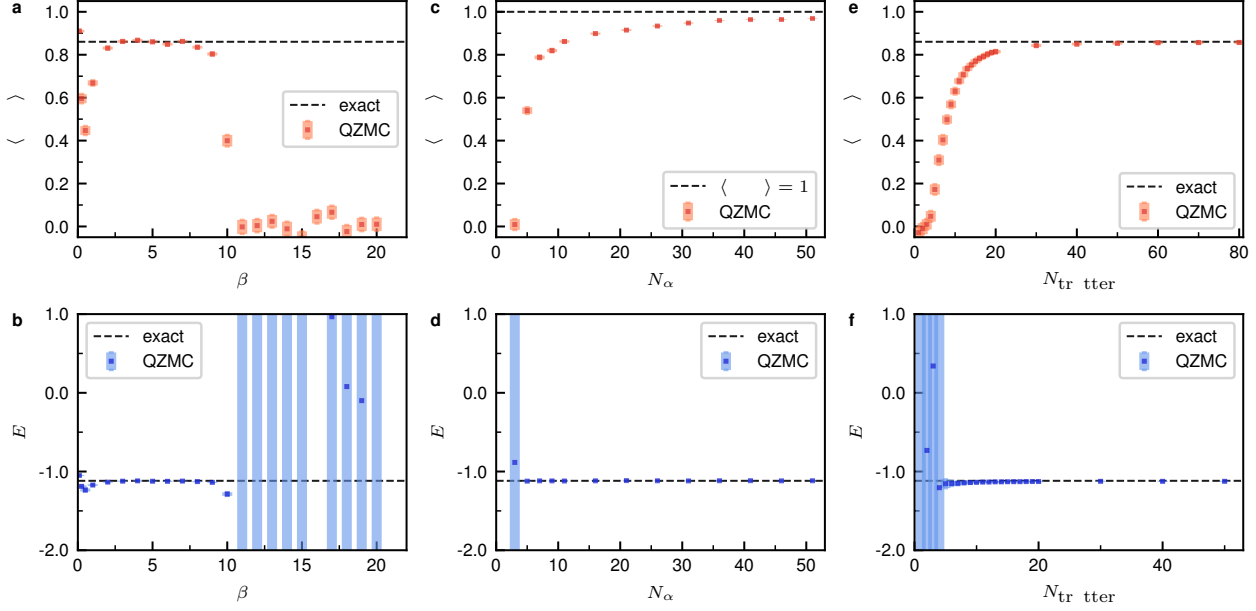


**Fig. S.5**  $|\beta$ ,  $N_\alpha$ , and  $N_T$  dependence of QZMC applied on the two-level system.  $\beta$  dependence of (a)  $\langle \Psi | \Psi \rangle$  and (b)  $E$ ,  $N_\alpha$  dependence of (c)  $\langle \Psi | \Psi \rangle$  and (d)  $E$ , and  $N_T$  dependence of (e)  $\langle \Psi | \Psi \rangle$  and (f)  $E$  for a ground state are plotted. In (a) and (b),  $N_\alpha = 10$  and we used the exact time evolution. For (c) and (d), we used  $\beta = 5$  and the exact time evolution. And (e) and (f) are computed with  $\beta = 5$  and  $N_\alpha = 10$ . In this figure, squares represents data points and shaded region is the numerically estimated error-bar. Here, We fixed  $N_\nu = 400$ .

from Eq. (S.47). Next, c and d depict the variation of  $\langle \Psi | \Psi \rangle$  and  $E$  with  $N_\alpha$ , showcasing convergence to exact values as  $N_\alpha$  increases, with  $E$  attaining accuracy as soon as  $\langle \Psi | \Psi \rangle$  takes a non-trivial value, at  $N_\alpha = 5$ . Finally, e-f display the results with trotterization, where the trotterized time evolution  $U(\lambda, \tau, N_T)$  for  $H(\lambda)$  is defined as

$$U(\lambda, \tau, N_T) = \prod_l^{N_T} e^{-i\Delta\tau X/2} e^{-i\Delta\tau(2\lambda-1)Z} \quad (\text{S.50})$$

with  $\Delta\tau = \tau/N_T$ . With increasing  $N_T$ ,  $\langle \Psi | \Psi \rangle$  converges to its exact value, while  $E$  converges to the exact values more rapidly, indicating the noise resilience of  $E$  in the presence of inaccurate time-evolution.

### 2.3 Hubbard dimer

Here, we demonstrate the application of QZMC to the Hubbard dimer using trotterized time evolution on an *ibm perth* quantum computer. We focus solely on the ground state for simplicity, employing second-order trotterization for the time evolution. For

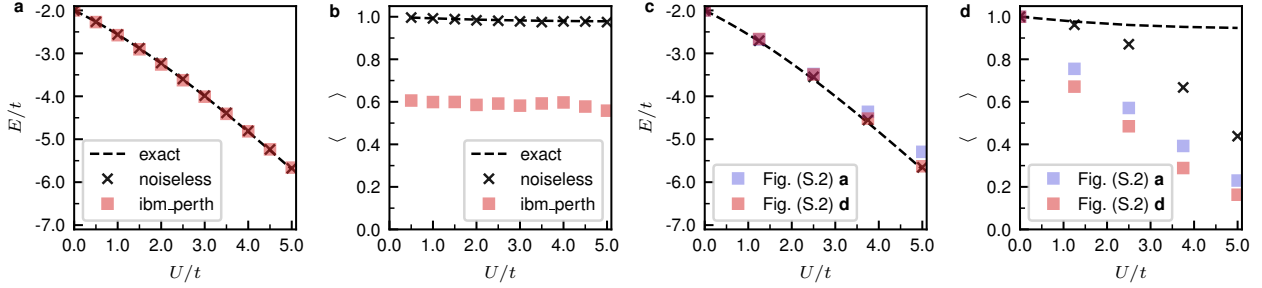


**Fig. S.6 | QZMC for the Hubbard dimer with the trotterized time evolution.** In **a** and **b**, we used compressed circuit (Fig. S.4 b), while the time evolution is computed with the trotter steps of 4. In **c** and **d**, we used uncompressed trotterized time evolutions. In **c** and **d**, red square calculated from the circuit Fig. S.2 d, while blue ones are calculated with Fig. S.2 a. In this figure, squares are computed using *ibm\_perth*, while gray crosses are for the noiseless simulation and the dotted line represent exact results. In every calculations, we used  $\beta = 0.5$ ,  $N_\nu = 100$ .

$H = H_1 + H_2$ , the second order trotterized time evolution  $U(\tau, N_T)$  is

$$U(\tau, N_T) = \prod_l^{N_T} e^{-i\Delta\tau H_1/2} e^{-i\Delta\tau H_2} e^{-i\Delta\tau H_1/2}. \quad (\text{S.51})$$

For Figure S.6 **a** and **b**, we employed the compressed circuit detailed in Fig.S.4 **b**. The trotterization using Eq. (S.51) is used with  $N_T = 4$  and  $H_1 = -\frac{U}{2}(I + Z_1 Z_2)$  and  $H_2 = -t(X_1 + X_2)$ . These figures illustrate the robustness of our algorithm even in the presence of both of trotterization errors and device noise. However, circuit compression may not always be feasible. To address this, we tested our algorithm with an uncompressed implementation of the trotterization. This approach notably reduces  $\langle \Psi | \Psi \rangle$  due to the increased circuit depth compared to the compressed version.

To manage this depth, we employed QZMC with a reference state (Fig.S.2). The reference state used was  $|\Psi_{\text{ref}}\rangle = [1/\sqrt{2} \ 0 \ 0 \ -1/\sqrt{2}]^T$ , representing the first excited state of the Hamiltonian. So, in Fig. S.6 **c** and **d**, we used  $N_\alpha = 4$ , with  $N_T = 1$ . We averaged two different trotterization choices (one with  $H_2 = -\frac{U}{2}(I + Z_1 Z_2)$  and the other with  $H_2 = -t(X_1 + X_2)$ ) as this choice significantly influences computational results when trotterization steps are small. We can see that, with the circuit Fig. S.2 **d**, QZMC gives accurate energy values, though it reduces  $\langle \Psi | \Psi \rangle$ . The circuits that we used for the QZMC with uncompressed trotterization are depicted in Figure S.7. Fig. S.7 **a** represents the initialization circuit, while Fig. S.7 **c** mimics the noise of the controlled-ZZ operation depicted in Figure S.7 **b**.

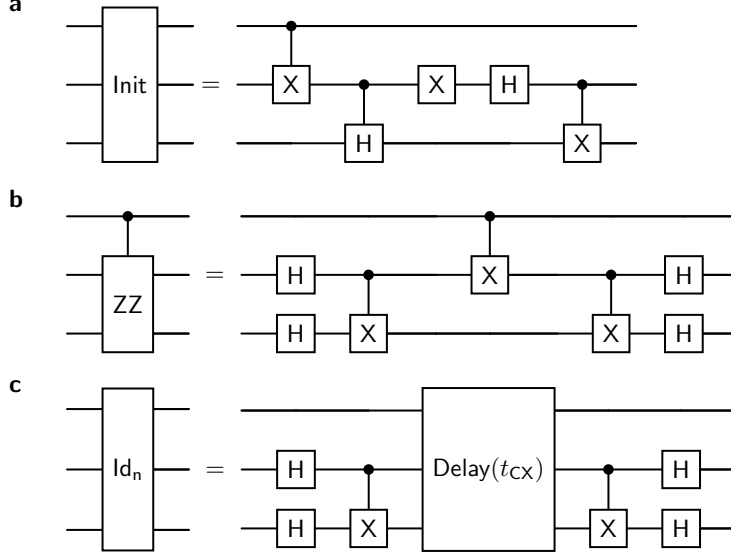


**Fig. S.7 | Quantum circuits for the Hubbard dimer** **a** is the initialization circuit for the ground state of the Hubbard dimer used in the QZMC with a reference state. The implementation of controlled-ZZ is drawn in **b**. To mimic error induced by controlled-ZZ, we used the noisy identity circuit **c**. In **c**,  $t_{CX}$  represent the duration that takes to CNOT operation the  $\text{Delay}(t)$  means the machine wait the duration of  $t$ .

### 3 Details of noiseless simulator calculations

Here, we discuss more detailed information of the large size Hubbard models considered in the main text. The Hubbard model is described by the Hamiltonian

$$H = - \sum_{\langle ij \rangle \sigma} t_{ij} c_{i\sigma}^\dagger c_{j\sigma} - \sum_i \mu (n_{i\uparrow} + n_{i\downarrow}) + \sum_i U n_{i\uparrow} n_{i\downarrow}. \quad (\text{S.52})$$

The first two terms represent the kinetic energy and are denoted as  $H_t$ , while the last term represents electron-electron interaction and is referred to as  $H_U$ . First, we present the quantum circuit for the ground state of the Hubbard dimer in Figure. S.8. Here, the angle  $\theta_d$  is given by

$$\theta_d = -2 \arctan \left( \frac{1}{2t} \left( \frac{U}{2} + \sqrt{\frac{U^2}{4} + 4t^2} \right) \right). \quad (\text{S.53})$$

In the simulation, we used  $N_\nu$  and trotter steps  $N_T$  that varies with system size, and we fixed the number of shots  $N_s = 10000$ . Based on Eq. (S.40), we determined  $N_\nu$  to be proportional to  $\|H'\|^2$ , which can be calculated as  $\|H'\| = t \times (\# \text{ of sites})$  for a chain and  $\|H'\| = 4t/\pi \times (\# \text{ of sites})$  for a ladder. And the proportionality constant is determined by testing  $6 \times 1$  system. The first order trotterized time evolution  $U_1(\tau)$

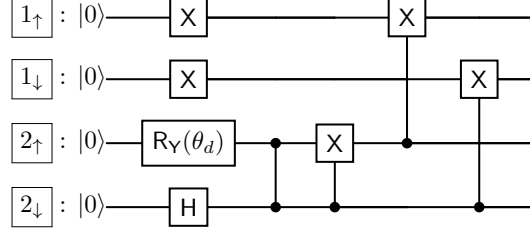


**Fig. S.8 | Quantum circuit for the ground state of the Hubbard dimer.** The Quantum circuit that prepares the ground state of the Hubbard dimer is depicted. Here,  $\theta_d$  is defined in Eq. (S.53).

of the Hubbard model with  $N_T$  trotter steps gives a Trotter error of [47]

$$\|e^{-iH\tau} - U_1(\tau)\| \leq \frac{\tau^2}{2N_T} \|[H_t, H_U]\|. \quad (\text{S.54})$$

Then,

$$\|[H_t, H_U]\| \leq \sum_{\langle ij \rangle > \sigma} t_{ij} U \| [c_{i\sigma}^\dagger c_{j\sigma}, \sum_i n_{i\uparrow} n_{i\downarrow}] \|. \quad (\text{S.55})$$

Since all orbital indices are equivalent,  $\|[c_{i\sigma}^\dagger c_{j\sigma}, \sum_i n_{i\uparrow} n_{i\downarrow}]\|$  remains constant for any  $i$  and  $j$ . Consequently,  $\|[H_t, H_U]\| \leq CU(t_{\text{intra}}N_{\text{intra}} + t_{\text{inter}}N_{\text{inter}})$  for some constant  $C$ .  $N_{\text{intra}}$  denotes the number of intra-dimer hoppings and  $N_{\text{inter}}$  represents the number of inter-dimer hoppings. Based on this, we determined  $N_T$  as

$$N_T = \text{int} \left[ 75 \times \frac{\beta^2 U (t_{\text{intra}}N_{\text{intra}} + t_{\text{inter}}N_{\text{inter}})}{9 \cdot 5 \cdot 8} \right] \quad (\text{S.56})$$

with a minimum  $N_T = 20$ .

We depict  $\langle \Psi | \Psi \rangle$  for Hubbard models in Figure S.9 a-f. These figures demonstrate that increasing  $N_\alpha$  proportionally to the number of sites yields similar values of  $\langle \Psi | \Psi \rangle$  across various Hubbard models we studied. Fig. S.9 g and h display spectral functions calculated with QZMC for 6-site Hubbard models.

## 4 State preparation for QZMC

Our method relies on the assumption that we have  $H_0$ , which can be easily solved with a classical computer, and that the eigenstate is readily preparable as a quantum circuit. However, arbitrary unitary synthesis can incur exponential quantum time costs [42], making the preparation of the eigenstate  $|\Phi_0\rangle$  challenging even when  $H_0$  can be exactly solved with a classical computer. In such cases, we prepare an easily accessible state  $|\tilde{\Phi}_0\rangle$  which has a non-trivial overlap with  $|\Phi_0\rangle$  (e.g.  $|\langle \Phi_0 | \tilde{\Phi}_0 \rangle|^2 > 0.5$ ). Then, we project  $|\tilde{\Phi}_0\rangle$  onto  $|\Phi_0\rangle$  at the first time by using Eq. (2) and perform QZMC in a

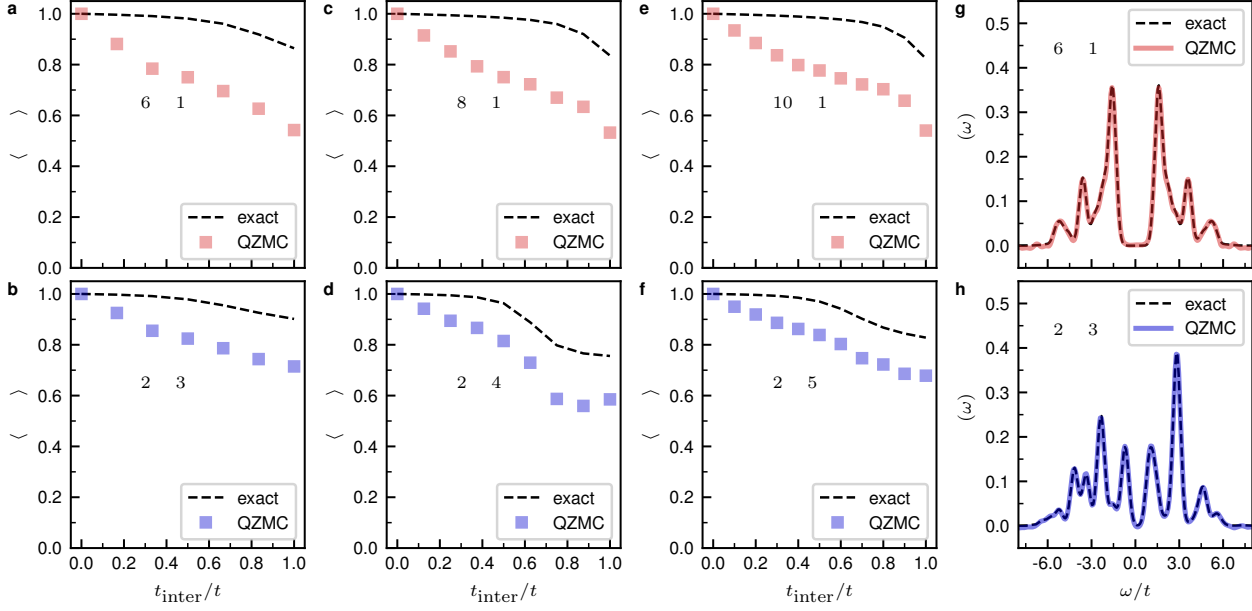


**Fig. S.9 | The half-filled Hubbard model in various sizes with QZMC.** We plotted the  $\langle \Psi | \Psi \rangle$  for various sized Hubbard model in **a-f**, and the spectral function for 6-site Hubbard models are plotted in **g** and **h**.

equivalent way. Therefore,

$$|\Psi_\alpha\rangle = \mathcal{P}_\alpha |\Phi_0\rangle \langle \Phi_0 | \tilde{\Phi}_0 \rangle, \quad (\text{S.57})$$

instead of Eq. (1). This costs  $N_\alpha \rightarrow N_\alpha + 1$  for the QZMC. As  $|\Phi_0\rangle$  is known and can be processed with a classical computer, finding  $|\tilde{\Phi}_0\rangle$  can be efficiently accomplished using classical computing resources.

## 5 Comparison with other works

Here, we compare the maximum time evolution length of QZMC with other methods under similar initial conditions. We prepared the initial state  $|\tilde{\Phi}_0\rangle$  with  $|\langle \Phi | \tilde{\Phi}_0 \rangle|^2 = 0.4$  and applied QZMC with Eq. (S.57). We fixed  $N_\alpha = 4$  and increased  $\beta$ . And we determined the maximum time evolution length of QZMC as  $C_{90}5\beta = 10.489\beta$ . Figure S.10a compares our approach with Ref. [15]. As shown in the figure, our method requires significantly smaller maximum time evolution length than the reference. Comparison with Ref. [17] and QPE is shown in Fig. S.10b. As depicted in the figure, our method requires a much smaller maximum time evolution length than QPE, and it is similar to Ref.[17].

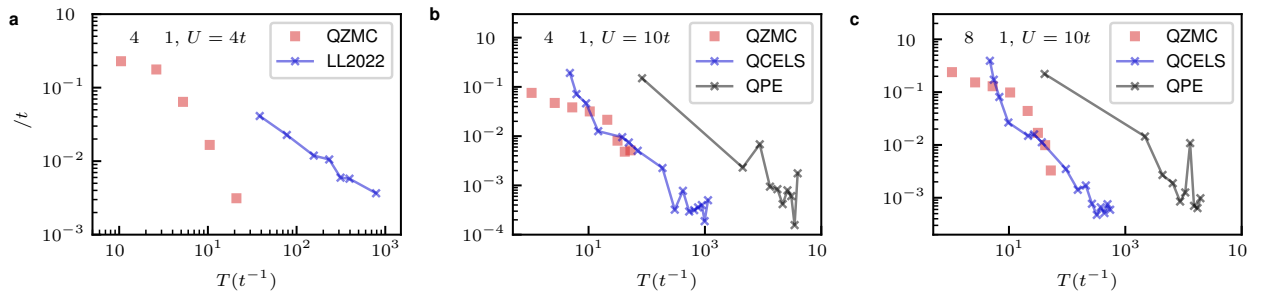


**Fig. S.10 | Comparison with other methods.** **a-c** plots ground state energy error  $\epsilon$  as a function of the maximum time evolution length  $T$ . **a** considers  $4 \times 1$  Hubbard model with  $U = 4t$ , **b** computes  $4 \times 1$  Hubbard model with  $U = 10t$ , and  $8 \times 1$  Hubbard model with  $U = 10t$  is considered in **c**. In **a**, blue points represents the data from Ref. [15]. And QCELS and QPE data in **b-c** are imported from Ref. [17] with unit conversion.